Susceptibility of F/A-18 Flight Control Laws to the Falling Leaf Mode

Part I: Linear Analysis

Abhijit Chakraborty [*], Peter Seiler [†] and Gary J. Balas[‡]

Department of Aerospace Engineering & Mechanics University of Minnesota , Minneapolis, MN, 55455, USA

The **F/A-18 Hornet** aircraft with the original flight control law exhibited an out-of-control phenomenon known as the falling leaf mode. Several **F/A-18 Hornet** aircraft were lost due to the falling leaf mode and this led **NAVAIR** and **Boeing** to redesign the flight control law. The revised flight control law exhibited successful suppression of the falling leaf mode during flight tests with aggressive maneuvers. This paper applies a variety of linear analysis methods to investigate the robustness properties of the original (baseline) and the revised flight control law at different trim points. Classical analyses, e.g. gain and phase margins, do not indicate a significant improvement in robustness properties of the revised control law over the baseline design. However, advanced robustness analyses, e.g. μ analysis, indicate that the revised control law is better able to handle the cross-coupling and variations in the dynamics than the baseline design.

[*]Graduate Research Assistant: `chakrab@aem.umn.edu`.

[†]Senior Research Associate: `seiler@aem.umn.edu`.

[‡]Professor: `balas@aem.umn.edu`.

American Institute of Aeronautics and Astronautics

Nomenclature

α = Angle-of-attack, rad

β = Sideslip Angle, rad

V = Velocity, $\frac{ft}{s}$

p = Roll rate, $\frac{rad}{s}$

q = Pitch rate, $\frac{rad}{s}$

r = Yaw rate, $\frac{rad}{s}$

ϕ = Bank angle, rad

θ = Pitch angle, rad

ψ = Yaw angle, rad

T = Thrust, lbf

ρ = Density, $\frac{slugs}{ft^3}$

$\bar{q}$ = Dynamic pressure, $\frac{lbs}{ft^2}$

m = Mass, $slugs$

g = Gravitational Constant, $\frac{ft}{s^2}$

a_y = Lateral acceleration, g

I. Introduction

The US Navy F/A-18 A/B/C/D Hornet aircraft with the baseline flight control law experienced a number of out-of-control flight departures since the early 1980's.[1,2] Many of these incidents were associated with a falling leaf mode instability of the aircraft.[2] The falling leaf mode is nonlinear in nature and poses a great challenge to understand its interaction with the flight control system. An extensive revision of the original (baseline) flight control law was performed by NAVAIR and Boeing in 2001 to suppress departure phenomenon, improve maneuvering performance and to expand the flight envelope of the vehicle.[2] The revised control law was implemented and successfully flight tested on the F/A-18 E/F Super Hornet aircraft. These flight tests included aggressive maneuvers that demonstrated successful suppression of the falling leaf motion by the revised control law.

Safety critical flight systems, like the F/A-18 Hornet or Super Hornet, require extensive validation prior to entry into service. The baseline flight control law of the F/A-18 Hornet aircraft was extensively tested prior to integration into the fleet without identifying the susceptibility of the aircraft to the falling leaf mode. This indicates that the current flight control system validation and verification techniques are not able to fully capture the nonlinear phenomenon, such as falling leaf, that the aircraft can experience.

This paper compares the linear robustness properties of the original (baseline) and the revised flight control law. Classical linear analyses, e.g. gain and phase margin, do not indicate a significant improvement

in robustness properties of the revised control law over the baseline design. However, advanced linear robustness analyses, e.g. μ analyses, indicate that the revised design is better able to handle the cross-coupling and variations in the dynamics than the baseline design. The falling leaf mode is a nonlinear phenomenon and cannot be duplicated with linear aircraft models. This motivates the need for additional nonlinear analysis to compare the baseline and revised flight control laws. A follow-on paper[3] describes a nonlinear robustness analysis method used to analyze the F/A-18 flight control laws.

This paper has the following structure. First, a six degree-of-freedom (DOF) mathematical model is derived for the F/A-18 Hornet aircraft. The aerodynamic model is represented as closed-form polynomial expressions, with functional dependence on the states. The falling leaf motion is described and simulation responses are presented showing the six DOF F/A-18 aircraft model captures the falling leaf characteristics. A simplified architecture of both the baseline and the revised flight control law are presented in Section III. Linear models suitable to analyze the falling leaf motion are derived. Both the closed-loop linear models are analyzed using classical techniques and linear robustness concepts such as the structured singular value (μ) and worst-case analysis in Section IV. The paper concludes with an overview of the paper.

II.   F/A-18 Aircraft Description and Model Development

The US Navy F/A-18 aircraft, Fig. 1[§], is a high performance, twin engine fighter aircraft built by the McDonnell Douglas (currently the Boeing Company) Corporation. The F/A-18-A/B and F/A-18-C/D are single and two seat aircraft, respectively. These variants are commonly known as Hornet. Each engine of the Hornet is a General Electric, F404-GE-400 rated at 16,100-lbf of static thrust at sea level. The aircraft features a low sweep trapezoidal wing planform with 400 ft^2 area and twin vertical tails.[4] Table 1 lists the aerodynamic reference and physical parameters of the F/A-18 Hornet.[4] The US Navy has experienced numerous mishaps, including loss of aircraft and pilot, over the life of the F/A-18A/B/C/D Hornet program due to a specific sustained out-of-control oscillatory motion known as the Falling Leaf mode.[2] A revision to the baseline F/A-18 Hornet flight control law was developed and successfully implemented on the F/A-18E/F Super Hornet aircraft in 2001. This revised flight control law has successfully suppressed the falling leaf motion.

A nonlinear mathematical model of the F/A-18 Hornet aircraft including its aerodynamic characteristics and control surface description is presented for the purpose of linear and nonlinear analysis of flight control system. Moreover, the Super Hornet has similar aerodynamic and inertial characteristics as of the Hornet.[2] Hence, the aerodynamic and inertial properties presented next are used to analyze both the baseline and the revised flight control system.

_____

§ Picture taken from http://www.dfrc.nasa.gov/Gallery/Photo/F-18Chase/Small/EC02-0224-1.jpg

American Institute of Aeronautics and Astronautics

Fig. 1. F/A-18 Hornet

Table 1. Aircraft Parameters

Wing Area, S	400 ft^2
Mean Aerodynamic Chord, $\bar{c}$	11.52 ft
Wing Span, b	37.42 ft
Mass, m	1034.5 slugs
Roll Axis Moment of Inertia, I_{xx}	23000 slug-ft^2
Pitch Axis Moment of Inertia, I_{yy}	151293 slug-ft^2
Yaw Axis Moment of Inertia, I_{zz}	169945 slug-ft^2
Cross-product of Inertia about y-axis, I_{xz}	-2971 slug-ft^2

A.   Control Surfaces

A conventional F/A-18 Hornet aircraft has five pairs of control surfaces: stabilators, rudders, ailerons, leading edge flaps (LEF), and trailing edge flaps (TEF). The leading and trailing edge flaps are used mostly during take-off and landing. Hence, these control effectors are not considered in the control analysis and modeling. Only the symmetric stabilator, aileron and rudder are considered as control effectors for the analyses performed in this paper. Note that the differential stabilator's contribution in roll-axis control is ignored in this paper for simplicity purpose. Longitudinal control or pitch axis control is provided by the symmetric deflection of the stabilators. Deflection of the ailerons is used to control the roll axis or lateral direction, and deflection of the rudders provides directional or yaw axis control. Note, The hydraulic actuation systems for these primary controls are modeled as first order lags. Table 2 provides the mathematical models of the actuators and their deflection and rate limits.[4] The actuator dynamics and rate/position limits are neglected in all analyses presented in this paper. Their values are only included for completeness.

Table 2. Control Surface and Actuator Configuration

Actuator	Rate Limit	Position Limit	Model
Stabilator, δ_{stab}	$\pm 40°/s$	$-24°,+10.5°$	$\frac{30}{s+30}$
Aileron, δ_{ail}	$\pm 100°/s$	$-25°,+45°$	$\frac{48}{s+48}$
Rudder, δ_{rud}	$\pm 61°/s$	$-30°,+30°$	$\frac{40}{s+40}$

B. Aerodynamic Model

The aircraft motion depends on the aerodynamic forces and moments acting on the vehicle. The aerodynamic forces consist of lift force (L in lbs), drag force (D in lbs), and sideforce (Y in lbs). The aerodynamic moments are described by the pitching moment (M in ft-lbs), rolling moment (l in ft-lbs), and yawing moment (n in ft-lbs). The aerodynamic forces and moments depend on the aerodynamic angles (α and β in rad), angular rates (p, q, r in rad/s) and control surface deflections (δ_{stab}, δ_{ail}, δ_{rud} in rad). These forces and moments are given by:

$$D = \bar{q}SC_D(\alpha,\beta,\delta_{stab}) \tag{1a}$$

$$L = \bar{q}SC_L(\alpha,\beta,\delta_{stab}) \tag{1b}$$

$$Y = \bar{q}SC_Y(\alpha,\beta,\delta_{ail},\delta_{rud}) \tag{1c}$$

$$l = \bar{q}SbC_l(\alpha,\beta,\delta_{ail},\delta_{rud},p,r,V) \tag{1d}$$

$$M = \bar{q}S\bar{c}C_M(\alpha,\delta_{elev},q,V) \tag{1e}$$

$$n = \bar{q}SbC_n(\alpha,\beta,\delta_{ail},\delta_{rud},p,r,V) \tag{1f}$$

where $\bar{q} := \frac{1}{2}\rho V^2$ is the dynamic pressure (lbs/ft^2) and ρ is the air density (lbs/ft^3). C_D, C_L, C_Y, C_l, C_M, and C_n are unitless aerodynamic coefficients. The functional form for the aerodynamic coefficients can be expressed as a sum of terms that model the aerodynamic effects of the basic airframe (C_*,basic), control inputs (C_*,control) and angular rate damping (C_*,rate). Here, C_* can be replaced by C_D, C_L, C_Y, C_l, C_M, C_n.

$$C_D(\alpha,\beta,\delta_{stab}) = C_{D,basic}(\alpha,\beta) + C_{D,control}(\alpha,\delta_{stab}) \tag{2a}$$

$$C_L(\alpha,\beta,\delta_{stab}) = C_{L,basic}(\alpha,\beta) + C_{L,control}(\alpha,\delta_{stab}) \tag{2b}$$

$$C_Y(\alpha,\beta,\delta_{ail},\delta_{rud}) = C_{Y,basic}(\alpha,\beta) + C_{Y,control}(\alpha,\delta_{rud},\delta_{ail}) \tag{2c}$$

$$C_l(\alpha,\beta,V,\delta_{ail},\delta_{rud}) = C_{l,basic}(\alpha,\beta) + C_{l,control}(\alpha,\delta_{rud},\delta_{ail}) + C_{l,rate}(\alpha,p,r,V) \tag{2d}$$

$$C_M(\alpha,\beta,V,\delta_{stab}) = C_{M,basic}(\alpha) + C_{M,control}(\alpha,\delta_{stab}) + C_{M,rate}(\alpha,q,V) \tag{2e}$$

$$C_n(\alpha,\beta,V,\delta_{ail},\delta_{rud}) = C_{n,basic}(\alpha,\beta) + C_{n,control}(\alpha,\delta_{rud},\delta_{ail}) + C_{n,rate}(\alpha,p,r,V) \tag{2f}$$

Due to lack of available data the rate damping effect on the aerodynamic force coefficients (C_D, C_L, C_Y)

American Institute of Aeronautics and Astronautics

is ignored in the model formulation. These force coefficients are modeled based only on contributions from the basic airframe and control surfaces.

A number of publications are available which provide flight test data for the stability and control derivatives of the F/A-18 HARV vehicle,[5–10] which has similar aerodynamic characteristics to the F/A-18 Hornet aircraft.[11] The aerodynamic data of the F/A-18 HARV is used to formulate the aerodynamic model for the F/A-18 Hornet. Least-square fitting of the flight data[5–10] is performed to derive a closed-form expression to the aerodynamic model. Appendix A provides the least squares fits for the aerodynamic coefficients.

There are two important issues associated with fitting the aerodynamic coefficients. First, the flight test data are provided over a range of 5 or 10° to 60° angle-of-attack with fewer data points at low angle-of-attack ($0^o \leq \alpha \leq 10^o$). Extrapolation of data within the lower range of angle-of-attack can lead to unrealistic fit which may lead to unrealistic aerodynamic characteristics at low angle-of-attack. For traditional aircraft, the aerodynamic characteristics of the vehicle do not change significantly at low angle-of-attack ($\alpha \leq 10^o$). Hence if data is unavailable, the aerodynamic coefficient is held constant for angle-of-attack between 0° and 10°.[12] The resulting model is valid for an angle-of-attack range from $0^o - 60^o$. Second, data is unavailable for nonzero sideslip flight conditions. However, the basic airframe coefficients are functionally dependent on both α, β. In this paper, the basic airframe dependence of C_Y, C_l, C_n, respectively $C_{Y,basic}(\alpha, \beta)$, $C_{l,basic}(\alpha, \beta)$, $C_{n,basic}(\alpha, \beta)$, in Eq. (2c), (2d), (2f), are approximated as $C_{Y,basic}(\alpha)\beta$, $C_{l,basic}(\alpha)\beta$, $C_{n,basic}(\alpha)\beta$ to account for this lack of data. This indicates, for C_Y, that the sideforce is expected to be zero when the sideslip is zero. This approximation step can also be viewed as linearization of the sideslip effect around the origin. Similar approach has been shown in the book by Stevens & Lewis.[13] Moreover, analytical expressions of $C_{D,basic}(\alpha, \beta)$, $C_{L,basic}(\alpha, \beta)$ are extracted from the thesis by Lulch.[7]

C. Equations of Motion

A six degree-of-freedom (DOF) 9-state mathematical model for the F/A-18 aircraft is presented in this section. The F/A-18 Hornet model is described by the conventional aircraft equations of motion.[9, 14, 15] The equations of motion take the form:

$$\dot{x} = f(x, u) \tag{3}$$

where $x := [V(\text{ft/s}), \ \beta(\text{rad}), \ \alpha(\text{rad}), \ p(\text{rad/s}), \ q(\text{rad/s}) \ r(\text{rad/s}), \ \phi(\text{rad}), \ \theta(\text{rad}), \ \psi(\text{rad})]$, and $u := [\delta_{ail}(\text{rad}), \ \delta_{rud}(\text{rad}), \ \delta_{stab}(\text{rad}), \ T(\text{lbf})]$. The equations of motion are provided next, without any formal derivation or detailed explanation. Note that the aerodynamic model and the equations of motion are presented in the units of radians. However, for ease of interpretation, results are presented in the units of degree in this paper.

Euler Angles

The rate of change of aircraft's angular positions are provided in Eq. (4).

$$
\begin{bmatrix} \dot{\phi} \\ \dot{\theta} \\ \dot{\psi} \end{bmatrix} = \begin{bmatrix} 1 & \sin\phi\tan\theta & \cos\phi\tan\theta \\ 0 & \cos\phi & -\sin\phi \\ 0 & \sin\phi\sec\theta & \cos\phi\sec\theta \end{bmatrix} \begin{bmatrix} p \\ q \\ r \end{bmatrix}
\tag{4}
$$

Force Equations

The aerodynamic forces, gravity forces and thrust force applied to the aircraft are considered. Thrust force is assumed to be constant. Eq. (5) defines the force equations.

$$
\dot{V} = -\frac{1}{m}(D\cos\beta - Y\sin\beta) + g(\cos\phi\cos\theta\sin\alpha\cos\beta + \sin\phi\cos\theta\sin\beta
$$
$$
- \sin\theta\cos\alpha\cos\beta) + \frac{T}{m}\cos\alpha\cos\beta
\tag{5a}
$$

$$
\dot{\alpha} = -\frac{1}{mV\cos\beta}L + q - \tan\beta(p\cos\alpha + r\sin\alpha)
$$
$$
+ \frac{g}{V\cos\beta}(\cos\phi\cos\theta\cos\alpha + \sin\alpha\sin\theta) - \frac{T\sin\alpha}{mV\cos\beta}
\tag{5b}
$$

$$
\dot{\beta} = \frac{1}{mV}(Y\cos\beta + D\sin\beta) + p\sin\alpha - r\cos\alpha + \frac{g}{V}\cos\beta\sin\phi\cos\theta
$$
$$
+ \frac{\sin\beta}{V}(g\cos\alpha\sin\theta - g\sin\alpha\cos\phi\cos\theta + \frac{T}{m}\cos\alpha)
\tag{5c}
$$

Moment Equations

The aerodynamic moments are associated with external applied moments. The gyroscopic effect of the moment is neglected. Eq. (6) describes the corresponding moment equations for the F/A-18 Hornet.

$$
\begin{bmatrix} \dot{p} \\ \dot{q} \\ \dot{r} \end{bmatrix} = \begin{bmatrix} \frac{I_{zz}}{\kappa} & 0 & \frac{I_{xz}}{\kappa} \\ 0 & \frac{1}{I_{yy}} & 0 \\ \frac{I_{xz}}{\kappa} & 0 & \frac{I_{xx}}{\kappa} \end{bmatrix} \left(\begin{bmatrix} l \\ M \\ n \end{bmatrix} - \begin{bmatrix} 0 & -r & q \\ r & 0 & -p \\ -q & p & 0 \end{bmatrix} \begin{bmatrix} I_{xx} & 0 & -I_{xz} \\ 0 & I_{yy} & 0 \\ -I_{xz} & 0 & I_{zz} \end{bmatrix} \begin{bmatrix} p \\ q \\ r \end{bmatrix} \right)
\tag{6}
$$

where $\kappa = I_{xx}I_{zz} - I_{xz}^2$

Eq. (4), (5), and (6) describe the mathematical model for the F/A-18 aircraft with the aerodynamic model presented in Section II.B. This is a standard mathematical representation for describing aircraft dynamics.

D. Falling Leaf

The original F/A-18A/B/C/D Hornet aircraft are susceptible to an out-of-control flight departure phenomenon with sustained oscillation namely 'falling leaf' motion. The falling leaf mode is briefly described in the following paragraph. A more detailed discussion of the falling leaf motion can be found in other references.[1,2]

The falling leaf motion of an aircraft can be characterized as large, coupled out-of-control oscillations in the roll rate(p) and yaw rate(r) direction combined with large fluctuations in angle-of-attack (α) and

American Institute of Aeronautics and Astronautics

sideslip (β).[1,2] Figure 2 shows the typical roll rate and yaw rate trajectories associated with the falling leaf motion.[1,2] This out-of-control mode exhibits periodic in-phase roll and yaw rates with large amplitude fluctuations about small or zero mean. Generation of the roll and yaw rate response is mainly due to the large sideslip oscillation. During large sideslip and angle-of-attack motion, the dihedral effect (roll caused by sideslip) of the aircraft wings becomes extremely large and the directional stability becomes unstable. The like-signs of these two components are responsible for the in-phase motion. The roll rate motion can easily reach up to $\pm 120°/s$, while the yaw rate motion can fluctuate around $\pm 50°/s$. During this motion, the value of angle-of-attack can reach up to $\pm 70°$ with sideslip oscillations between $\pm 40°$.[1] The required aerodynamic nose-down pitching moment is exceeded by the pitch rate generation due to the inertial coupling of the in-phase roll and yaw rates. The reduction in pitching moment is followed by a reduction in normal force, eventually causing a loss of lift in the aircraft. Another distinguishing feature of the falling leaf motion is the time response of α vs. β produces a mushroom shape curve as shown in Fig. 3.
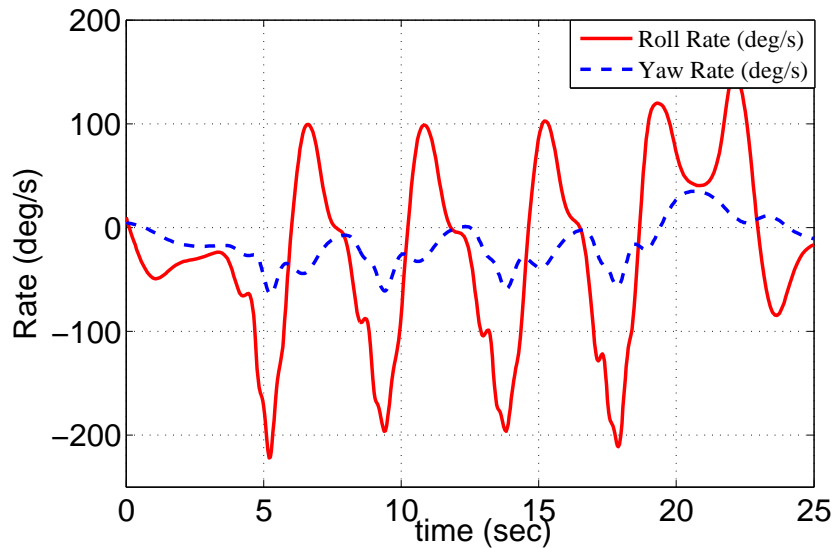

Fig. 2. **Large and coupled roll rate - yaw rate oscillation during falling leaf motion**

The characteristics of the falling leaf motion are nonlinear in nature. Figures 2 and 3 are generated by simulating the nonlinear F/A-18 model presented in this paper. The falling leaf motion shown in Fig. 2 and 3 are generated with the following initial condition.

$$x_o := [350 \text{ (ft/s) } 20^o \ 40^o \ 10^o/s \ 0^o/s \ 5^o/s \ 0^o \ 0^o \ 0^o] \tag{7}$$

Note that units of degree are used for ease of interpretation. The model presented in this paper uses the unit of radian. The ordering of the states x are same as mention in Eq. 3. The inputs are set to zeros for this particular simulation. Note that the falling leaf responses cannot be generated by simulating the linearized models as described later in Section IV.A.

A study of the falling leaf motion[1] has categorized the motion into three different spectrum: (i) slow falling leaf, (ii) fast falling leaf, and (iii) high alpha fast falling leaf. The primary differences in shifting from
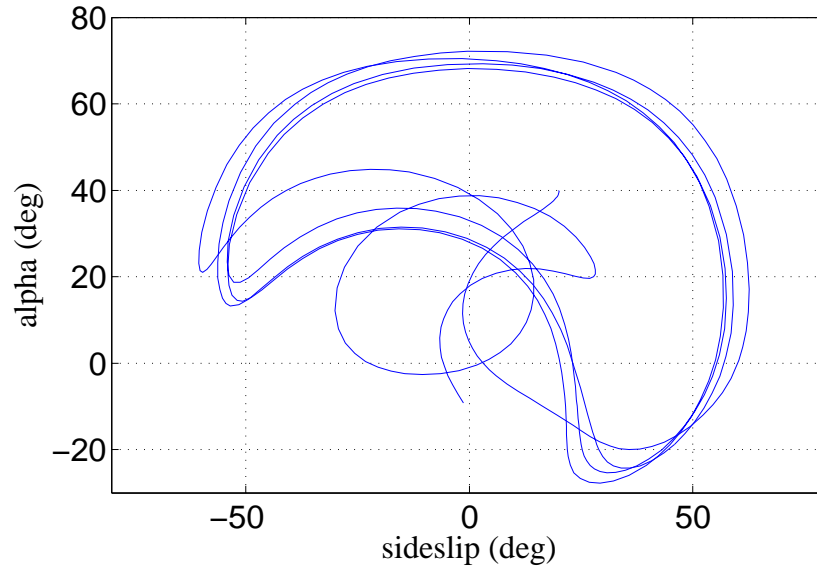
Fig. 3. **Time response of α vs. β produces a mushroom shape curve during falling leaf motion**

the slow to the fast mode can be contributed to the movement of α to higher values, the biasing of yaw rate, and an increase in the frequency of the oscillation. Table 3 categorizes the three falling leaf motion as reported in the study.[1] The analyses presented in this paper are closely related to the slow falling leaf mode category.

Table 3. **Falling Leaf Categories**

State	Slow Mode	Fast Mode	High α Mode
α(deg)	-5 to $+60$	$+20$ to $+70$	$+30$ to $+85$
β(deg)	-40 to $+40$	-40 to $+40$	-40 to $+40$
p(deg/s)	-120 to $+150$	-90 to $+130$	-90 to $+130$
r(deg/s)	-50 to $+50$	-10 to $+60$	-10 to $+75$
period(s)	7	4.7	4.5
frequency(rad/s)	0.898	1.34	1.39

III.   F/A-18 Flight Control Laws

Numerous aggressive flight tests of the Super Hornet indicated the suppression of the 'falling leaf' motion under the revised flight control law.[2] A simplified architecture of the baseline flight control law is presented in Section III.A and the revised flight control law is presented in Section III. B. Appendix B provides the state-space realization for both control laws.

American Institute of Aeronautics and Astronautics

A. Baseline Control Law

Figure 4 shows the control law architecture for the baseline control laws used for analysis in this paper. The baseline controller structure for the F/A-18 aircraft closely follows the *Control Augmentation System (CAS)* presented in the report by Buttrill, Arbuckle, and Hoffler.[4] The actuators have fast dynamics, as mentioned in Table 2, and their dynamics can be neglected without causing any significant variation in the analysis results. Hence, the actuator dynamics, presented in Table 2, are ignored for analysis purposes. Differences between the control structure presented in this paper and the report by Buttrill, Arbuckle, and Hoffler[4] are described in the following sections.
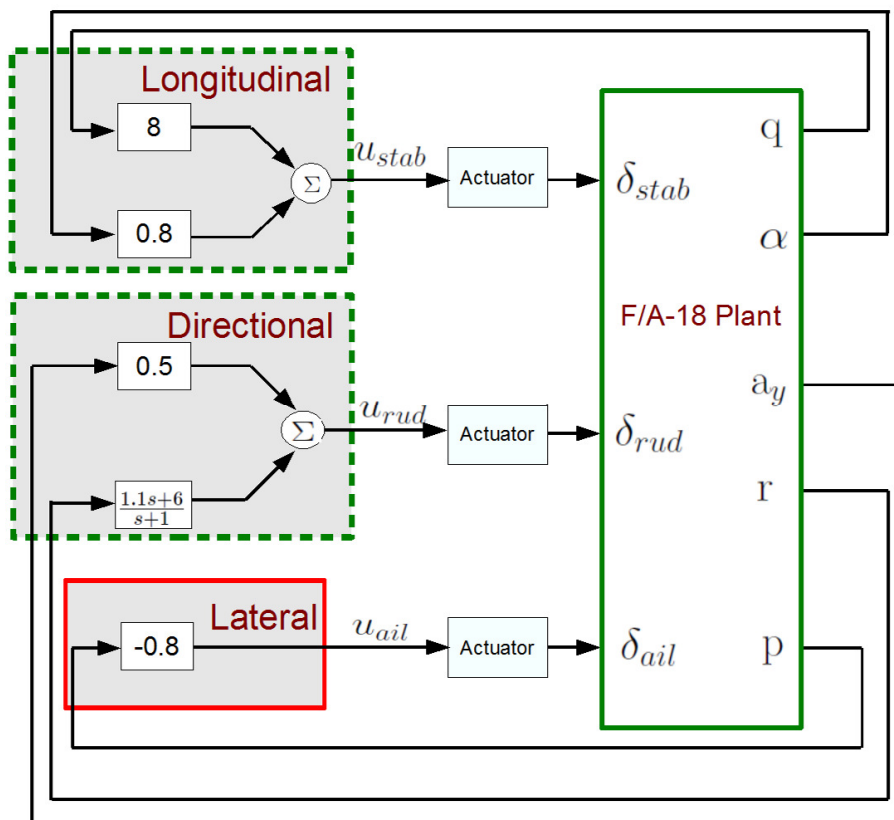

Fig. 4. F/A-18 Baseline Flight Control Law

1. Longitudinal Control

The longitudinal baseline control design for the F/A-18 aircraft includes angle-of-attack (α in rad), normal acceleration (a_n in g), and pitch rate (q in rad/s) measurement feedback. The angle-of-attack feedback is used to stabilize an unstable short period mode that occurs during low speed, high angle-of-attack maneuvering. The inner-loop pitch rate feedback is comprised of a proportional feedback gain, to improve damping of the short-period mode. In the high speed regime, the pitch rate proportional gain needs to be increased to avoid any unstable short period mode. The normal acceleration feedback, a proportional-integrator (PI)

American Institute of Aeronautics and Astronautics

compensator, has not been implemented in the simplified control law structure. The normal acceleration feedback is usually implemented to stabilize any unstable short period mode of the aircraft. This short period stabilization is provided by α or q feedback in the simplified control law structure presented in this paper. Hence, the normal acceleration feedback is ignored.

2. Lateral Control

Control of the lateral direction axis involves roll rate (p) feedback to the aileron actuators. Roll rate feedback is used to improve roll damping and the roll-subsidence mode of the aircraft. Due to the inherent high roll damping associated with the F/A-18 aircraft at high speed, the roll rate feedback authority is usually reduced at high dynamic pressure. In the low speed regime, the roll rate feedback gain is used to increase damping of the Dutch roll mode. The roll rate feedback gain ranges between 0.8 at low speed to 0.08 at high speed. The flight conditions considered in the analysis in this paper are at a forward velocity of 350 ft/s. At this speed, a feedback gain of 0.8 is used to provide roll damping.

3. Directional Control

Directional control involves feedback from yaw rate (r) and lateral acceleration (a_y) to the rudder actuators. Yaw rate is fed back to the rudder to generate a yawing moment. Yaw rate feedback reduces the yaw rate contribution to the Dutch-roll mode. In a steady state turn, there is always a constant nonzero yaw rate present. This requires the pilot to apply larger than normal rudder input to negate the effect of the yaw damper and make a coordinated turn. A washout filter is used to effectively eliminate this effect. The filter approximately differentiates the yaw rate feedback signal at low frequency, effectively eliminating yaw rate feedback at steady state conditions.[13] The lateral acceleration feedback contributes to reduce sideslip during turn coordination.

B. Revised Control Law

Figure 5 shows the architecture of the revised F/A-18 flight control law as described in the papers by Heller, David, & Holmberg[2] and Heller, Niewoehner, & Lawson.[16] The objective of the revised flight control law was to improve the departure resistance characteristics and full recoverability of the F/A-18 aircraft without sacrificing the maneuverability of the aircraft.[2] The significant changes in the revised control law are the additional sideslip (β) and sideslip rate ($\dot{\beta}$) feedback to the aileron actuators.

There are no direct measurements of sideslip and sideslip rate. The sideslip and the sideslip rate feedback signals are computed based on already available signals from the sensors and using the kinematics of the aircraft. Specifically, sideslip rate ($\dot{\beta}$) is estimated by using a 1st order approximation to the sideslip state derivative equation. The sideslip feedback plays a key role in increasing the lateral stability in the $30 - 35^o$ range of angle-of-attack. The sideslip rate feedback improves the lateral-directional damping. Hence, sideslip motion is damped even at high angles-of-attack. This feature is key to eliminating the falling leaf mode
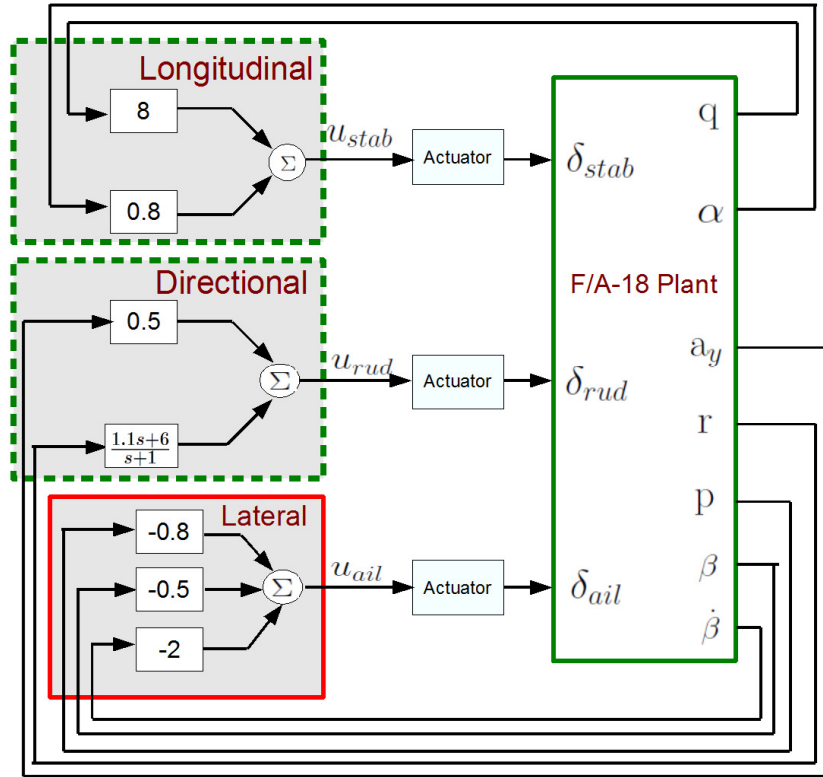
American Institute of Aeronautics and Astronautics

Fig. 5. F/A-18 Revised Flight Control Law

behavior of the aircraft, which is an aggressive form of in-phase Dutch-roll motion. Proportional feedback is implemented in these two feedback channels. The values of the proportional gains are $k_\beta = 0.5$ and $k_{\dot\beta} = 2$.

IV.   Linear Analysis

Current practice for validating flight control laws relies on applying linear analysis tools to assess the closed loop stability and performance characteristics about many trim conditions. Linear analysis investigates robustness issues and possibly worst-case scenarios around the operating points. In this paper, the F/A-18 aircraft is trimmed around different operating points of interest that are suitable to characterize the falling leaf motion. A reduced 6-state linear representation is extracted from the 9-state linear models around these operating points. This 6-state linear representation is used to construct the closed-loop models for both the baseline and revised flight control law for linear robustness analysis.

A.   Linear Model Formulation

Linear models are formulated around selected operating points. The flight conditions for these operating points are chosen such that the aircraft is likely to experience the falling leaf motion. Section II.D characterized the falling leaf motion similar to the aggressive dutch roll motion with strong coupling in all three axes: longitudinal, lateral and directional. Flight conditions that exhibit coupling in all three directions are

American Institute of Aeronautics and Astronautics

suitable candidates for analyzing the falling leaf motion. Therefore, steady-level flight conditions are not considered in the analysis. However, bank angle maneuvers exhibit coupling in all three directions and are suitable to analyze the falling leaf motion. In this paper, both coordinated ($\beta = 0$ deg) and uncoordinated ($\beta \neq 0^o$) turns with 0°, 10°, 25°, 35° bank angle are considered. Simulation results[1] have shown the velocity of the aircraft is usually within 250 - 350 ft/s during the falling leaf motion. The F/A-18 aircraft is trimmed around $V_t = 350$ ft/s. Table 4 provides the trim values for the flight conditions considered in this paper. The subscript 't' denotes the trim value.

Table 4. Trim Values around $V_t = 350\frac{ft}{s}$ altitude $=25,000$ ft

State/Input	Plant 1	Plant 2	Plant 3	Plant 4	Plant 5	Plant 6	Plant 7	Plant 8
α_t (deg)	15.29	15.59	17.43	20.29	15.59	16.16	18.41	21.40
β_t (deg)	0	0	0	0	10	10	10	10
ϕ_t (deg)	0	10	25	35	0	10	25	35
p_t (deg/s)	0	0.1322	0.8695	1.845	-0.1478	-0.5188	-1.074	-1.353
r_t (deg/s)	0	0.7500	1.864	2.635	0.3276	1.084	2.141	2.821
q_t (deg/s)	0	0.1322	0.8695	1.845	0	0.1911	0.9982	1.975
θ_t (deg)	26.10	25.67	22.98	18.69	24.27	25.24	24.45	21.45
ψ_t (deg)	0	0	0	0	0	0	0	0
δ_{Stab_t} (deg)	-2.606	-2.683	-3.253	-4.503	-2.669	-2.823	-3.606	-5.101
δ_{Ail_t} (deg)	0	-0.1251	-0.3145	-0.4399	12.21	12.45	13.72	15.60
δ_{Rud_t} (deg)	0	-0.3570	-0.9109	-1.359	13.24	12.73	11.22	8.334
T_t (lbf)	14500	14500	14500	14500	14500	14500	14500	14500

The F/A-18 aircraft is linearized around the trim points specified in Table 4. The linearized plants have the following form:

$$\dot{x} = Ax + Bu \tag{8}$$

$$y = Cx + Du \tag{9}$$

where x, u are described in Section II.C and y denotes the output, $y := [a_y,\ p,\ r,\ \alpha,\ \beta,\ q,\ \dot{\beta}]$. Recall, $a_y = \frac{\bar{q}S}{mg}C_y$ and $\dot{\beta}$ is computed based on already available signals from the sensors and using the kinematics of the aircraft. In this paper, the linearized equations for both a_y and $\dot{\beta}$ are used as output signals. Appendix C provides the linear state-space data for Plant 4 and Plant 8 presented in Table 4.

A six-state representation of the F/A-18 model is extracted from the above 9-state model, described in Eq. (8). Decoupling the three states V, θ, ψ from the 9-state linear model results in the following 6-state model with the thrust input held constant at the trim value.

American Institute of Aeronautics and Astronautics

$$\dot{x}_6 = Ax_6 + Bu_3 \tag{10}$$

$$y = Cx_6 + Du_3 \tag{11}$$

where $x_6 := [\beta, \ \alpha, \ p, \ q, \ r, \ \phi]$ and $u_3 := [\delta_{ail}, \ \delta_{rud}, \ \delta_{stab}]$.

Table 5 shows the eigenvalues of the linear plant (Plant 4) with 9-state and 6-state representation. The zero eigenvalue in the 9-state linear plant is due to the heading angle (ψ) state, which does not affect the dynamics. This state can be ignored in formulating the reduced (6-state) linear plant for analysis. Moreover, the eigenvalues indicate that the dynamic modes of a standard aircraft are present in the F/A-18 linear model. The dynamic modes of the aircraft are: short-period and phugoid mode in the longitudinal axes and dutch roll, roll subsidence and spiral mode in the lateral directional axes. The phugoid mode in the longitudinal direction involves V and θ states. The period of this mode ($T_p \approx 50.3 \ s$) is separated by more than an order of magnitude to the one of the short-period ($T_p \approx 3.79 \ s$), as shown in Table 5. This large time scale separation rationalizes that the phugoid mode can be decoupled from the aircraft model and yet retain the important characteristics of the other dynamic modes of the aircraft.

Table 5. Eigenvalue of the F/A-18 Linear Plant

Mode	9-State		6-State	
	Eigenvalue	Period (s)/ Time Constant (s)	Eigenvalue	Period (s)/ / Time Constant (s)
Short Period	-0.195 ± 1.66	3.79	-0.194 ± 1.66	3.79
Phugoid	-0.0509 ± 0.125	50.3	N/A	N/A
Dutch Roll	-0.202 ± 0.918	6.85	-0.203 ± 0.933	6.73
Roll Subsidence	-0.307	3.25	-0.302	3.31
Spiral	-0.0209	47.8	-0.0515	19.4
Heading Angle	0	0	N/A	N/A

The rationale for decoupling the V, θ states can also be seen by examining the frequency response of the linear models. Figure 6 shows a Bode plot of the magnitude response for both the 9-state and 6-state model representation from the stabilator channel input to the six states (x_6). The removal of states V and θ do not affect the aileron and rudder channel as much as the stabilator channel. The Bode phase plot is also shown in Fig. 7. Recall, the frequency for the slow falling leaf motion is approximately 0.9 rad/s, as shown in Table 3. Moreover, the magnitude and phase plots show that the 6-state approximation is a good approximation in the interested falling leaf region, above 0.9 rad/s. The two models differ in the low frequency (≤ 0.9 rad/s) region. The mismatch in low frequency region between the two models is deemed acceptable in terms of capturing the characteristics of the falling leaf motion.

The lateral-directional modes are important to capture the in-phase roll-yaw oscillation characteristics of
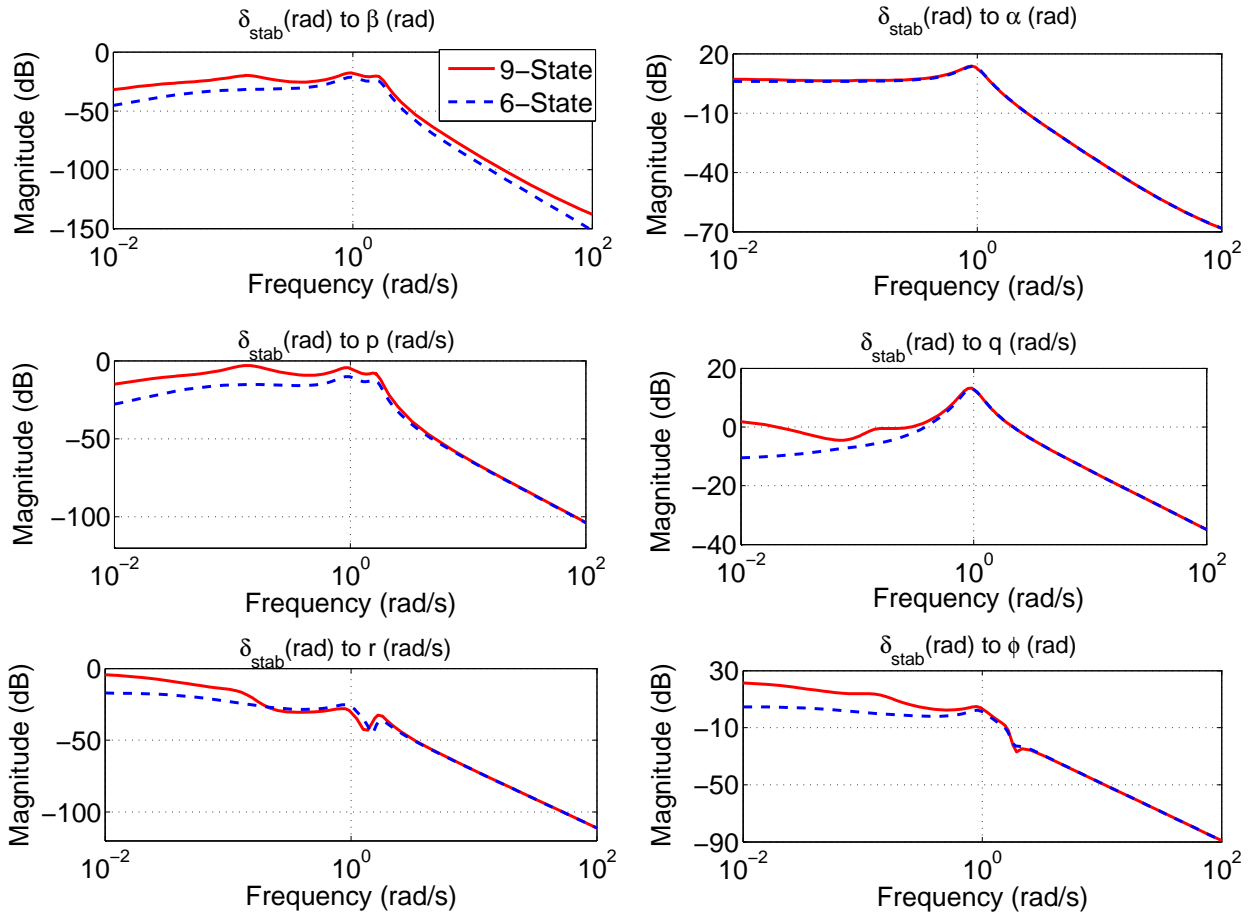
Fig. 6. Bode plot: Magnitude comparison between the 9-state and 6-state representation

the falling leaf motion. Hence, these dynamic modes (dutch roll, roll subsidence and spiral mode) involving β, p, r, ϕ states are kept in the formulation of the linear plant. The longitudinal states α, q are also retained in order to capture the short-period mode. Table 5 provides the eigenvalue characteristics of the two linear representation. The reduced 6-state representation retains the dynamic modes of the aircraft, excluding the phugoid mode.

Six state linear models are constructed for each of the eight operating points. These 6-state linear representations are used to construct the closed-loop model for the baseline and revised flight control law. Eight closed-loop systems are formulated for each of the flight control law; four plants for coordinated turn and four associated with an uncoordinated turn. A variety of linear robustness concepts are employed in Section IV.B - IV.D to compare the stability performance between the baseline and the revised flight control law.

B. Loop Margin Analysis

Gain and phase margins are classical measures of robustness for the closed-loop system. A typical requirement for certification of a flight control law requires the closed-loop system to achieve at least $6dB$ of gain margin
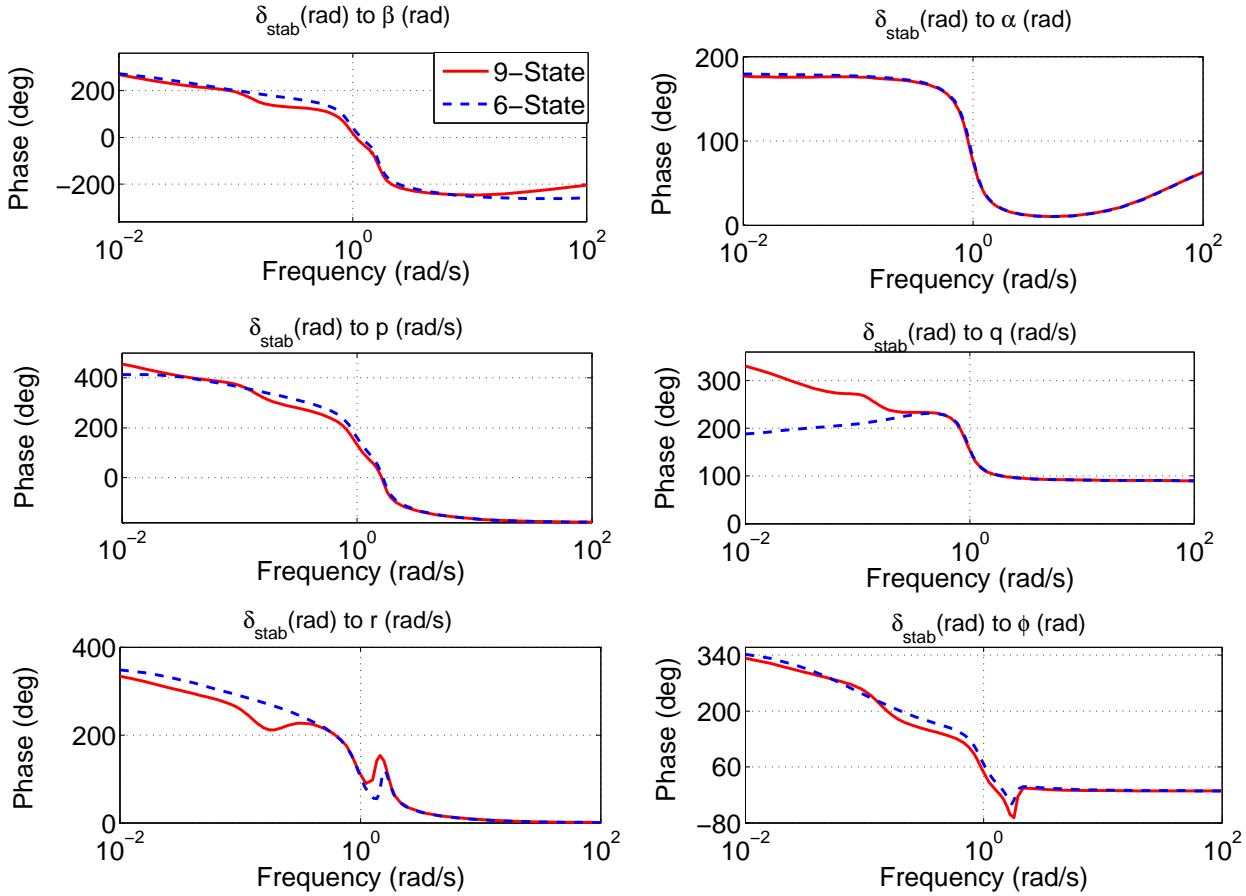
American Institute of Aeronautics and Astronautics

Fig. 7. Bode plot: Phase comparison between the 9-state and 6-state representation

and 45° of phase margin. The F/A-18 aircraft closed-loop plants under consideration are multivariable; hence, both disk margin and multivariable margin analyses are also performed in addition to the classical loop-at-a-time margin analysis.

1.   Classical Gain, Phase and Delay Margin Analysis

Classical gain, phase and delay margins provide robustness margins for each individual feedback channel with all the other loops closed. This loop-at-a-time margin analysis provides insight on the sensitivity of each channel individually. Table 6 provides the classical margins for both the baseline and the revised flight control laws. The results, presented in Table 6, are based on the uncoordinated ($\beta = 10^o$) bank turn maneuver at $\phi = 35^o$ (Plant 8). This plant results in the worst margins among all the other plants mentioned in Table 4. The baseline and revised flight control laws have very similar classical margins at the input channel. Both the flight control laws are very robust and satisfy the minimum requirement of $6dB$ gain margin and 45° phase margin.

American Institute of Aeronautics and Astronautics

Table 6. Classical Gain & Phase Margin Analysis for Plant 8

Input Channel		Baseline	Revised
Aileron	Gain Margin	43.4 dB	37.1 dB
	Phase Margin	∞	93.6^o
	Delay Margin	∞	0.399 sec
Rudder	Gain Margin	21.8 dB	21.7 dB
	Phase Margin	69.5^o	70.8^o
	Delay Margin	2.00 sec	1.38 sec
Stabilator	Gain Margin	∞	∞
	Phase Margin	90.4^o	90.4^o
	Delay Margin	0.110 sec	0.110 sec

2. Disk Margin Analysis

Disk margin analysis provides an estimate of the single-loop robustness to combined gain/phase variations.[17] The disk margin metric is very similar to an exclusion region on a Nichols chart. As with the classical margin calculation, coupling effects between channels may not be captured by this analysis. Table 7 provides the disk gain and phase variations at each loop for both the control laws. The results are based on the uncoordinated bank turn maneuver at $\phi = 35^o$ (Plant 8). Again, both the flight control laws achieve similar robustness margin which exceed the desired requirements. The disk margins of the two flight control laws are nearly identical.

Table 7. Disk Margin Analysis for Plant 8

Input Channel		Baseline	Revised
Aileron	Gain Margin	43.4 dB	37.1 dB
	Phase Margin	89.2^o	88.4^o
Rudder	Gain Margin	7.15 dB	7.92 dB
	Phase Margin	42.6^o	46.2^o
Stabilator	Gain Margin	∞	∞
	Phase Margin	90°	90°

3. Multivariable Disk Margin Analysis

The multivariable disk margin indicates the robustness of the closed-loop system to simultaneous (across all channels), independent gain and phase variations. This analysis is conservative since it allows independent variation of the input channels simultaneously. Figures 8 and 9 presents the multivaribale disk margin
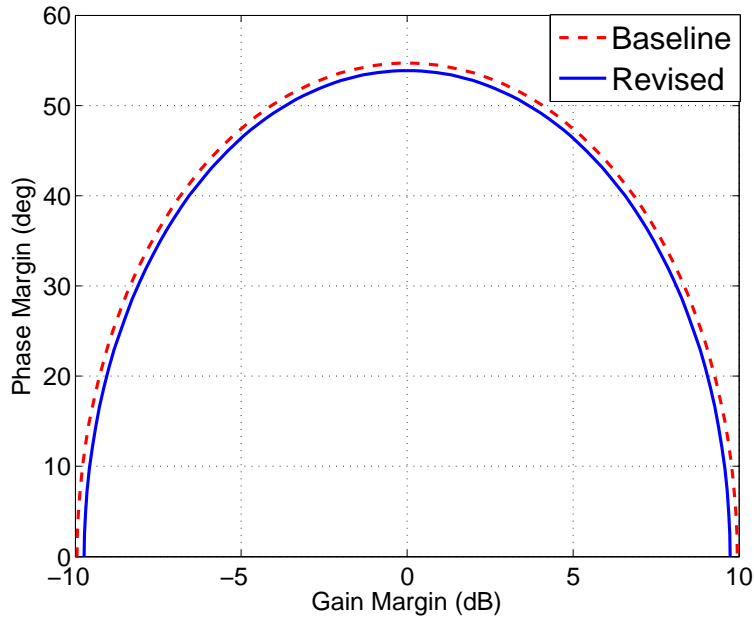
American Institute of Aeronautics and Astronautics

Fig. 8. Multivariable disk margin analysis for coordinated 35° bank angle turn

ellipses, respectively for plant 4 (coordinated turn at 35° bank angle) and plant 8 (uncoordinated turn at 35° bank angle). The mutivariable disk margin analysis certifies that for simultaneous gain & phase variations in each channel inside the region of the ellipses the closed-loop system remains stable. The mutivariable disk margin analysis for steady bank turn maneuvers, Fig. 8, shows both the baseline and the revised flight control laws have similar multivariable margins. In fact, the baseline appears to have slightly better margin than the revised flight control law. For this steady maneuver, both the control laws are robust to gain variation of up to $\approx \pm 9.5$ dB and phase variation of $\approx \pm 54^o$ across channels. Figure 9 shows the mutivariable disk margin analysis for unsteady bank turn maneuvers. Here, the revised flight control law has a slightly better margin than the baseline flight control law. However, the differences in the margins between the two control laws is not significant enough to conclude which flight control law is susceptible to the falling leaf motion. Moreover, both the control laws achieve the typical margin requirement specification (6dB gain margin and 45° phase margin) for the steady maneuver. For the unsteady maneuvers, the gain margin requirement is satisfied (both achieves slightly over 6 dB), but the achieved phase margin ($\approx 40^o$) falls short of the requirement.

C. Unmodeled Dynamics: Input Multiplicative Uncertainty

Modeling physical systems accurately in many engineering applications is a challenge. A mathematical model of the physical system usually differs from the actual behavior of the system. The F/A-18 aircraft model presented in this paper is no exception. One approach is to account for the inaccuracies of the modeled aircraft dynamics by unmodeled dynamics entering at the input to the system.

Figures 10 shows the general uncertainty structure of the plant that will be considered in the input multiplicative uncertainty analysis. To assess the performance due to the inaccuracies of the vehicle modeled,
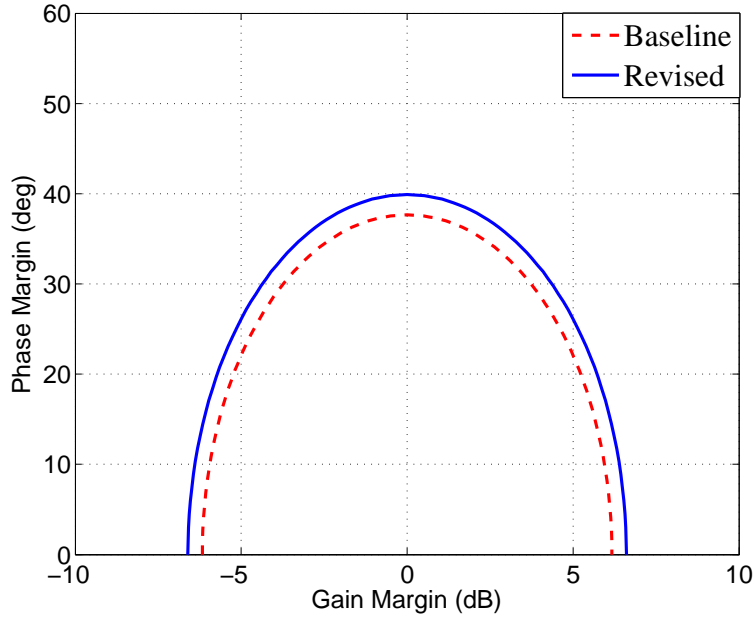
American Institute of Aeronautics and Astronautics

Fig. 9. Multivariable disk margin analysis for uncoordinated 35° bank angle turn with 10° sideslip angle

multiplicative uncertainty, $W_I \Delta_{IM}$, in all three input channels is introduced. The uncertainty Δ_{IM} represents unit norm bounded unmodeled dynamics. The weighting function is set to unity for analysis purpose, $W_I = I_{3\times3}$. The structured singular value (μ) will be used to analyze the uncertain closed-loop system. The $\frac{1}{\mu}$ value measures the stability margin due to the uncertainty description in the system.
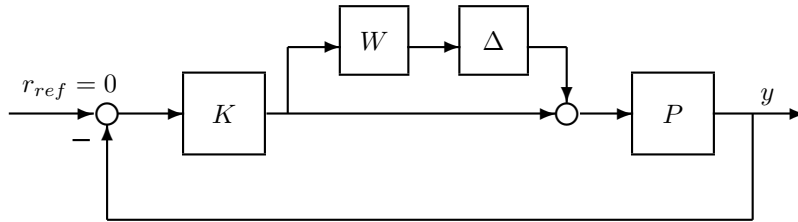
Fig. 10. F/A-18 Input Multiplicative Uncertainty Structure

1. Diagonal Input Multiplicative Uncertainty

Figures 11 and 12 show the μ plot of the baseline and revised closed-loop system for coordinated (plants 1-4) and uncoordinated (plants 5-8) bank maneuvers for the interconnection structure shown in Fig. 10. The uncertainty, Δ_{IM}, is assumed to have a diagonal structure indicating the presence of uncertainty in each actuation channel but no cross-coupling among the channels. The value of μ at each frequency ω is inversely related to the smallest uncertainty which causes the feedback system to have poles at $\pm j\omega$. Thus the largest value on the μ plot is equal to $1/k_m$ where k_m denotes the stability margin. In Fig. 11, the peak value of μ is 1.150 ($k_m = 0.8695$) for the revised controller during steady maneuvers. The baseline achieves a peak value of μ is 1.030 ($k_m = 0.9708$). The baseline flight control law achieves a slightly better robustness for the

American Institute of Aeronautics and Astronautics

coordinated bank turn maneuvers compared to the revised flight control law. Figure 12 shows the peak value of μ for both the control laws at uncoordinated bank turn maneuvers. Here, the baseline flight controller exhibits a peak μ value of 1.894 ($k_m = 0.5279$) and the revised flight controller achieves a μ value of 1.816 ($k_m = 0.5506$). During the uncoordinated maneuvers, the revised controller achieves better stability margins than the baseline design.
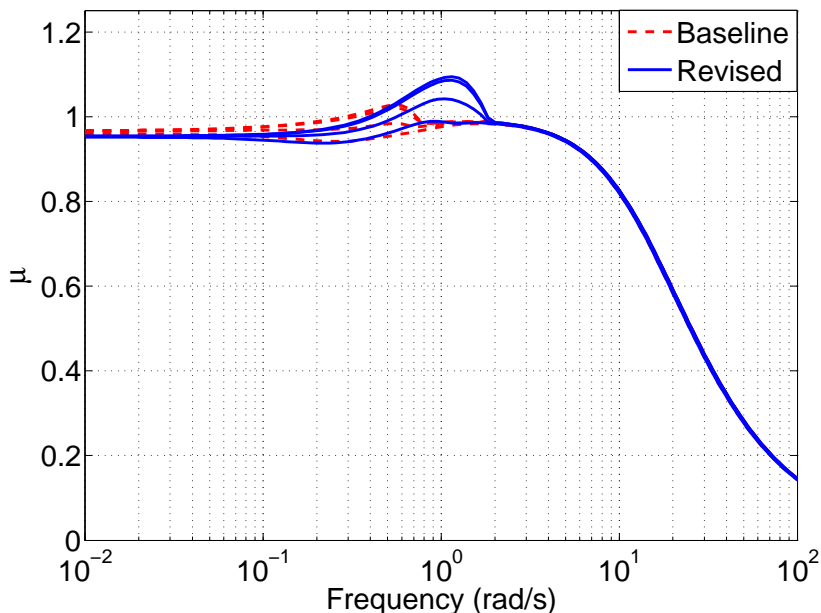

Fig. 11. **Diagonal Input Multiplicative Uncertainty: Coordinated maneuvers**

Both the flight control laws exhibit similar robustness or stability margins under diagonal input multiplicative uncertainty for both the coordinated and uncoordinated maneuvers. Overall, the stability margins of both the control laws are excellent and nearly identical.

2. Full Block Input Multiplicative Uncertainty

The input multiplicative uncertainty, Δ_{IM}, is treated as a full block uncertainty in the analysis. This uncertainty structure models the effects of dynamic cross-coupling between the channels to determine how well the flight control laws are able to handle the coupling at the input to the F/A-18 actuators. As mentioned before, the falling leaf motion is an exaggerated form of in-phase Dutch-roll motion with large coupling in the roll-yaw direction. Increased robustness of the flight control law with respect to the full Δ_{IM} is associated with its ability to mitigate the onset of the falling leaf motion. Figure 13 presents robustness results for coordinated maneuvers (plants 1-4), and Fig. 14 presents results for uncoordinated (plants 5-8) maneuvers.

Figure 13 shows the μ analysis for coordinated maneuvers. In this case, the baseline flight control law achieves a peak μ value of 1.846 ($k_m = 0.5417$) and the revised flight control law achieves a peak μ value of 1.220 ($k_m = 0.8196$). The results indicate the revised flight control law is more robust as compared to the baseline flight control law. Similarly, Fig. 14 shows the μ analysis for uncoordinated maneuvers. The
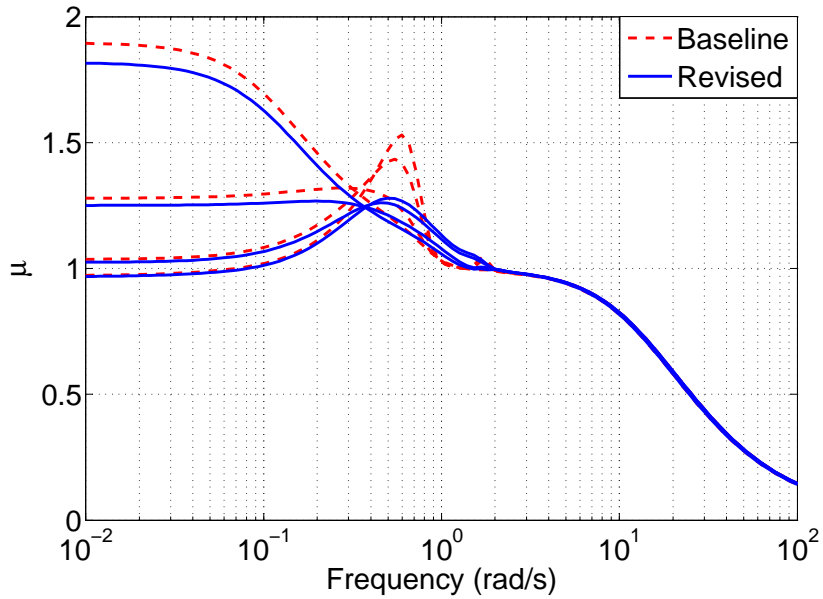
American Institute of Aeronautics and Astronautics

Fig. 12. Diagonal Input Multiplicative Uncertainty: Uncoordinated maneuvers

baseline flight control law achieves a peak μ value of 3.075 ($k_m = 0.3252$) and the revised flight control law achieves a peak μ value of 2.032 ($k_m = 0.4921$).
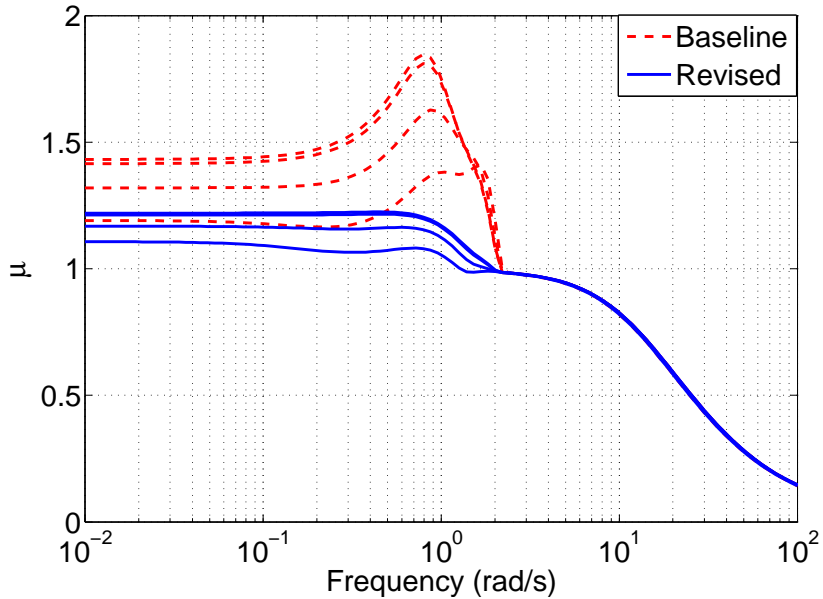

Fig. 13. Full Block Input Multiplicative Uncertainty: Coordinated maneuvers

Linear robustness analysis with respect to full-block input multiplicative uncertainty across input channels indicate the revised controller is more robust than the baseline design. This implies that the revised controller is better able to handle cross-coupling in the actuation channels. Moreover, both Fig. 13 and 14 show the revised controller provides additional damping to the system around approximately 1 rad/s, while the baseline
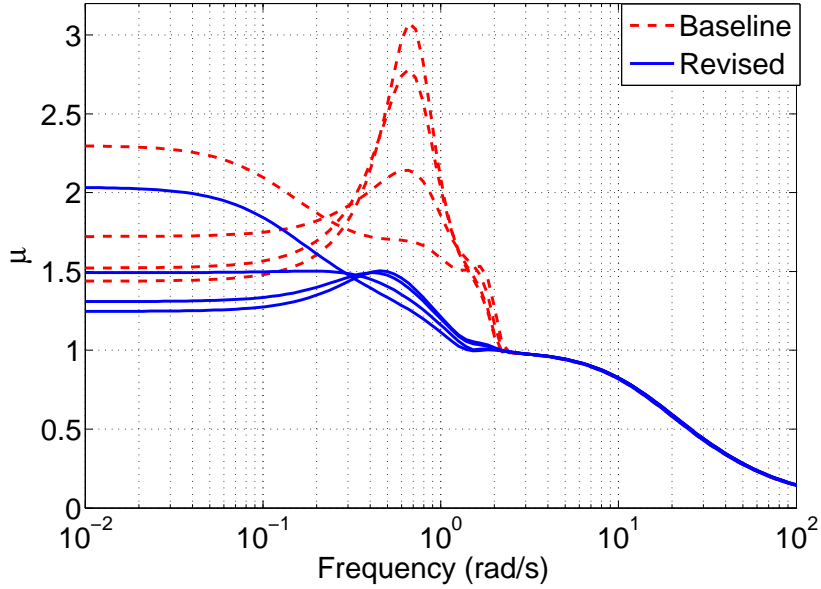
American Institute of Aeronautics and Astronautics

Fig. 14. Full Block Input Multiplicative Uncertainty: Uncoordinated maneuvers

peaks up around that frequency. To summarize, the full-block uncertainty analysis indicates a noticeable improvement in the robustness properties of the revised control law over the baseline control law.

D.   Robustness Analysis to Parametric Uncertainty

Robustness analysis of flight control system with parametric uncertainty is another important analysis in validating closed-loop robustness and performance.[18] Moreover, robustness assessment of the flight control law due to the variations of aerodynamic coefficients over the flight envelope needs to be considered. Including parametric uncertainty models into the analysis is one approach to address this issue. Both controllers are examined with respect to robustness in the presence of parametric variations in the plant model. To this end, the stability derivatives of the linearized model are represented with $\pm 10\%$ uncertainty around their nominal values. These perturbed coefficients are chosen carefully to represent the stability characteristics of the F/A-18 aircraft that play an important role in the falling leaf motion. These terms are related to the entries of the linearized open-loop A matrix. The terms in the lateral directions are: sideforce due to sideslip (Y_β); rolling moment due to sideslip (L_β); yawing moment due to sideslip (N_β); roll damping (L_p); yaw damping (N_r). The following longitudinal terms have also been considered: pitch damping (M_q); normal force due to pitch rate (Z_q); pitch stiffness (M_α). Cook[15] provides a detailed description of these terms. The lateral aerodynamic terms: Y_β, L_β, N_β, L_p, and N_r correspond respectively to the $(1,1)$, $(3,1)$, $(5,1)$, $(3,3)$, and $(5,5)$ entries of the linearized A matrix presented in previous section. The longitudinal aerodynamic terms: M_q, Z_q, and M_α correspond respectively to the $(4,4)$, $(2,4)$, and $(4,2)$ entries of the same linearized A matrix.

Figures 15 and 16 show the μ plot of both closed-loop systems with respect to the parametric uncertainty
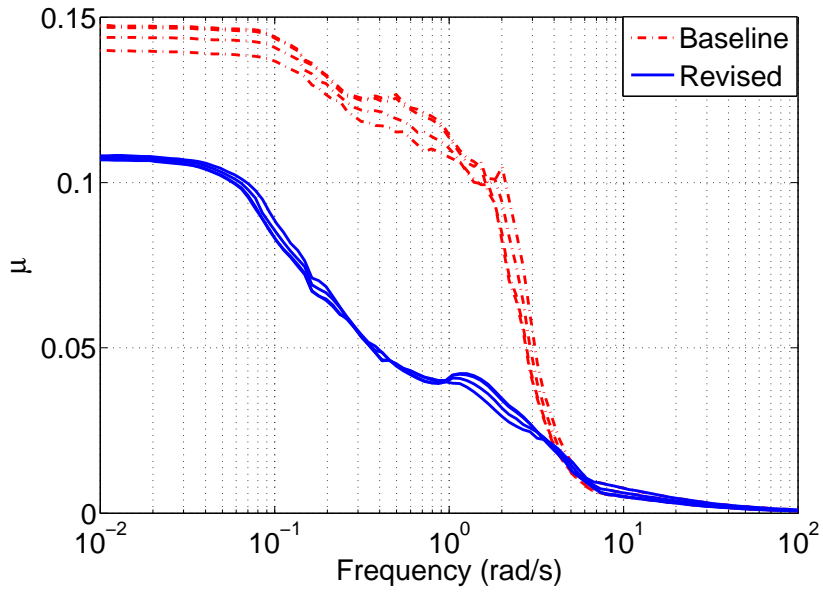
Fig. 15. Real Parametric Uncertainty in Aerodynamic Coefficients: Coordinated maneuvers
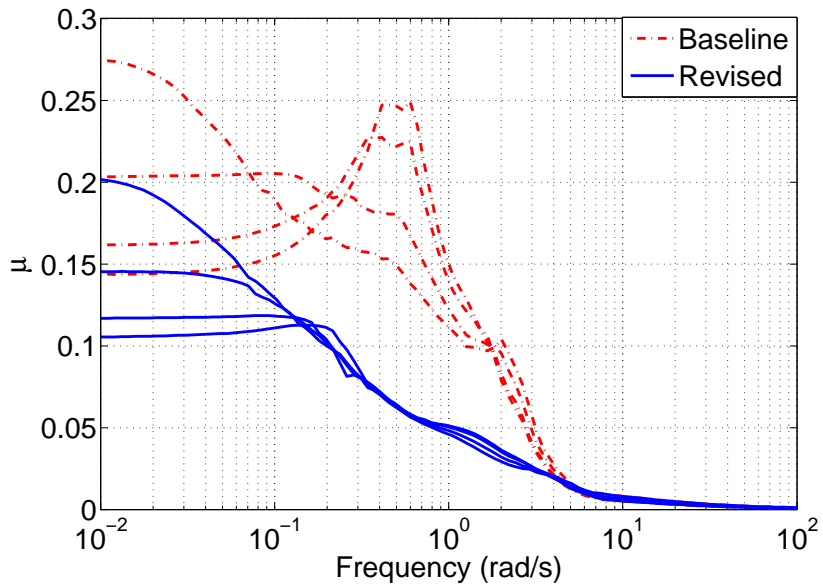

Fig. 16. Real Parametric Uncertainty in Aerodynamic Coefficients: Uncoordinated maneuvers

for both coordinated (plants 1-4) and uncoordinated maneuvers (plants 5-8), respectively. In Fig. 15, the stability margin for parametric uncertainty in the aerodynamic coefficients of the revised controller ($\mu = 0.1080$ and $k_m = 9.259$) is approximately 1.3 times larger than that of the baseline controller ($\mu = 0.1475$ and $k_m = 6.779$). Figure 16 presents results based on plants 5-8 for uncoordinated ($\beta = 10^o$) maneuvers. In Fig. 16, the stability margin for parametric uncertainty in the aerodynamic coefficients of the revised controller ($\mu = 0.2016$ and $k_m = 4.960$) is approximately 1.3 times larger than that of the baseline controller

American Institute of Aeronautics and Astronautics

($\mu = 0.2746$ and $k_m = 3.642$). Hence, the revised flight controller is more robust to uncertainty in aerodynamic derivatives than the baseline design. This is specifically true for the uncoordinated turns. With uncoordinated banking maneuvers, the μ value for the baseline flight control law peaks up around 0.7 rad/s, while the revised design does not exhibit the peaking behavior. However, both the flight controllers prove to be very robust against the parametric uncertainty in the stability derivatives.

E. Worst-Case Analysis of Flight Control Laws

The ability of the revised flight control law to damp out the sideslip motion, even during high AOA maneuvers, is key in suppressing the falling leaf motion.[2] This motivates a comparison between the worst-case performance of the two flight control laws due to disturbances in aileron and rudder channel, uncertainty in the stability derivatives, and their effect on the sideslip. Figure 17 shows the setup of the problem formulation. The 1-by-2 transfer function of interest is from disturbances in the aileron and rudder channels to sideslip output. P_Δ is the the uncertain plant with uncertainty being represented as: (i) parametric uncertainty in aerodynamic coefficients, and (ii) unmodeled dynamics uncertainty.
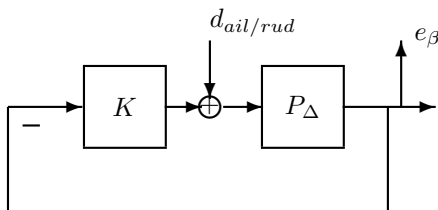

Fig. 17. Setup of worst-case analysis: 'd' indicates the disturbances in rudder and aileron channel and 'e_β' indicates the Sideslip channel

1. Worst-Case Parametric Uncertainty Analysis

The uncertainty, in this case, is associated with stability derivatives of the plant as described in Section IV.D. Figure 18 shows a frequency-dependent μ plot of the worst-case gain analysis from the sideslip feedback channel to the aileron and rudder input channel for the coordinated maneuvers. Comparatively, the revised flight control law performs better than the baseline flight control law. The baseline flight control achieves a peak worst-case gain of 1.30 while the revised flight control law achieves a worst-case gain of 0.675. Figure 19 shows μ plot of the worst-case gain curve for uncoordinated maneuvers. In this case, the revised flight control law performs substantially better than the baseline design. The worst-case gain of the baseline control law is 2.41 while the revised achieves a value of 0.748.

In both maneuvers, the revised flight control law damps out the peak in the worst-case gain in sideslip direction while the baseline fails to do so. This analysis shows that the revised control law is better able to handle worst-case uncertainty scenarios with respect to the aerodynamic parameter variations in the dynamics.
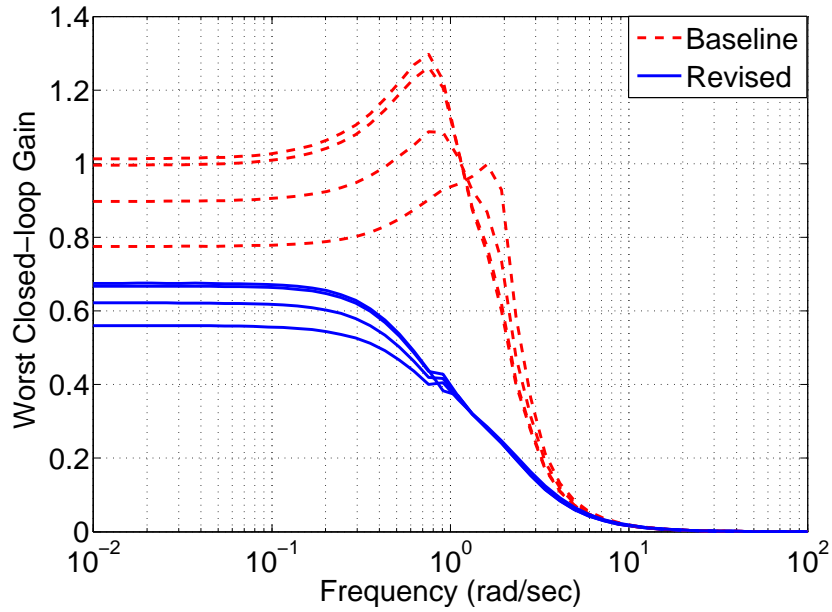
American Institute of Aeronautics and Astronautics

Fig. 18. Worst-Case closed loop gain as a function of frequency under parametric variations: Coordinated maneuvers
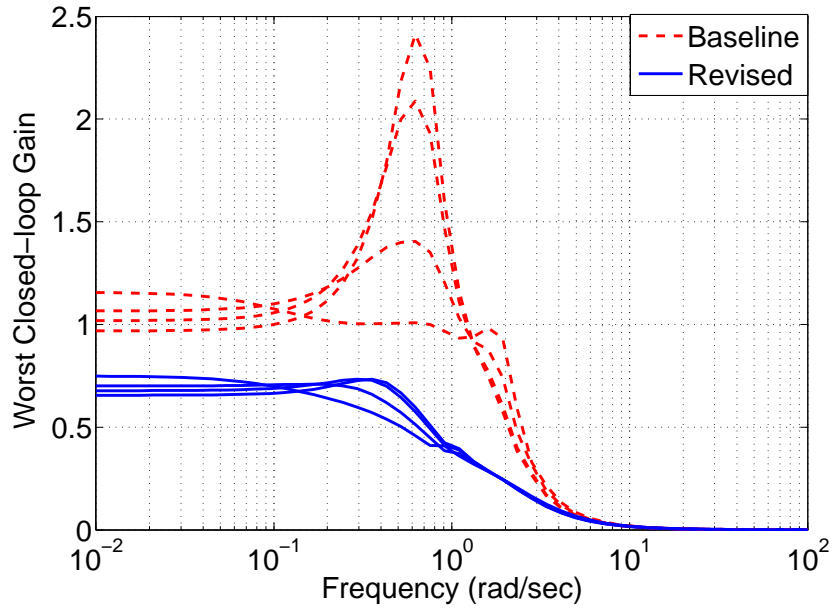

Fig. 19. Worst-Case closed loop gain as a function of frequency under parametric variations: Uncoordinated maneuvers

2. Unmodeled Dynamics: Diagonal Input Multiplicative Uncertainty

The unmodeled dynamics uncertainty is modeled in the actuation channel with no cross-coupling (diagonal input multiplicative uncertainty) between them, as described in Section IV.C. The results turn out to be similar for the full-block input multiplicative uncertainty case. Hence, only diagonal input multiplicative uncertainty results are presented.

American Institute of Aeronautics and Astronautics

In the diagonal input multiplicative uncertainty case for the coordinated maneuvers, the baseline flight control law achieves a slightly higher worst-case gain value compared to the revised flight control law. The revised controller achieves a worst-case gain of 4.12 while the baseline design achieves a gain of 4.70. Figure 20 shows the frequency dependent wort-case gain curve of the disturbance rejection properties of the flight control laws. Moreover, Fig. 21 shows the worst-case gain curve for the uncoordinated maneuvers. In this flight condition, the worst-case gain for both the baseline and the revised flight control law is same. Both the baseline and the revised achieved similar robustness properties for the worst-gain analysis with unmodeled dynamics uncertainty.
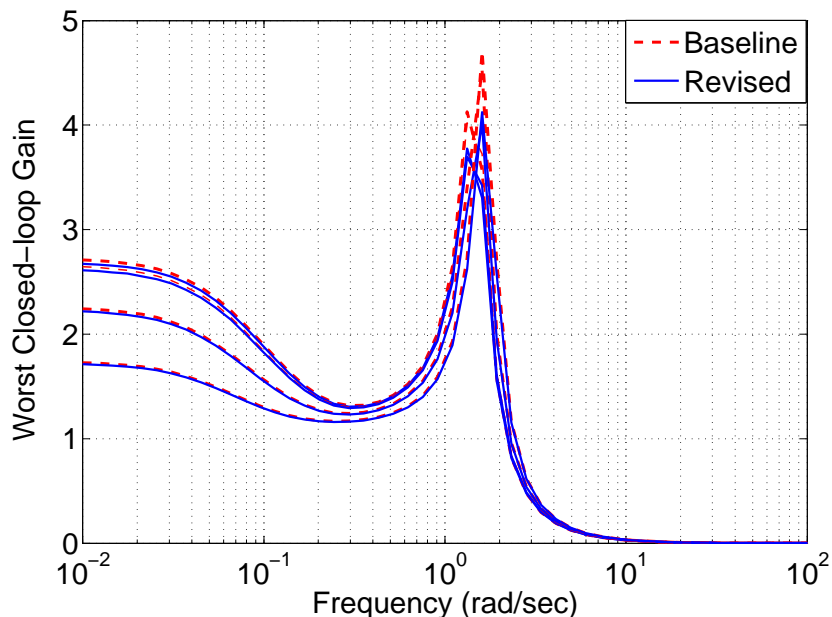

Fig. 20. Worst-Case closed loop gain as a function of frequency under unmodeled dynamics uncertainty: Coordinated maneuvers

F. Summary of Linear Analysis Results

Section IV.B - IV.E employs various linear analysis techniques to compare the robustness properties of the baseline and the revised flight control laws. The standard loop margin analysis, performed in Section IV.B, shows both the controllers achieve almost identical robustness margin and are very robust. Various μ analyses are performed in the following subsections with different uncertainty structure in the aircraft plant. Section IV.C analyzes both the controller under the presence of unmodeled dynamics uncertainty in the actuation channel. Both the controllers achiever similar robustness properties under no cross-coupling in the actuation channels. However, the revised design achieves better robustness properties when cross-coupling is modeled in the actuation channels. Similarly, in Section IV.D, the revised controller achieves better robustness margin under variations in the aerodynamic coefficients. Finally, the worst-case gain analysis is performed in Section IV.E. The worst-case closed-loop gain for the revised controller turns out to be less than the baseline design under variations in aerodynamic coefficients. However, both the controllers achieve
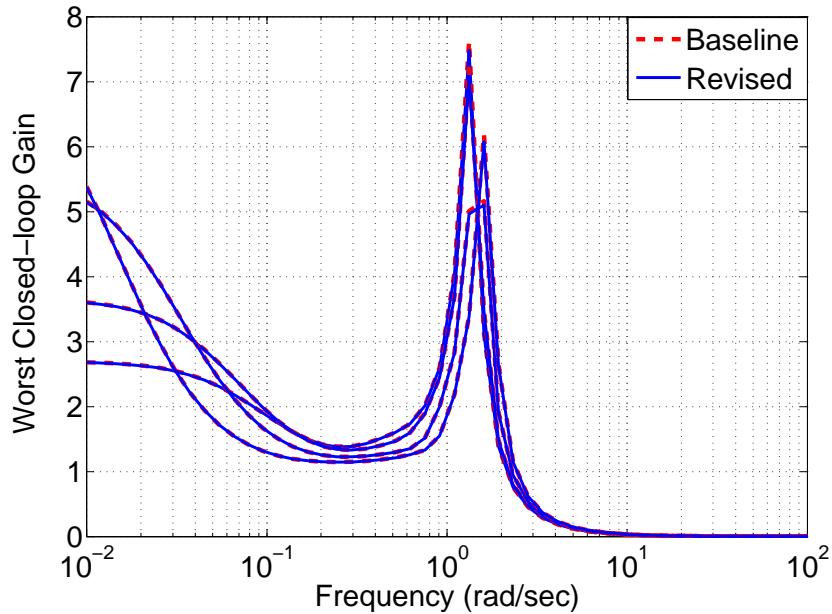
American Institute of Aeronautics and Astronautics

Fig. 21. Worst-Case closed loop gain as a function of frequency under unmodeled dynamics uncertainty: Uncoordinated maneuvers

similar worst-case closed-loop gain under unmodeled dynamics uncertainty in the actuation channels.

The flight test results have shown that the revised control law is able to damp out the falling leaf motion while the baseline controller failed to do so. Gain and phase margin analysis is extensively used during the certification of the flight control law. These classical analyses do not indicate any significant difference in the robustness properties between the two control laws. The advance linear analyses did indicate a significant improvement in the robustness properties of the revised control law. In particular, a full block uncertainty at the plant input models cross-coupling effects at the plant input and analyses with this uncertainty model indicated a significant difference between the two control laws. This analysis motivates the use of advanced linear robustness analysis tools in the validation and verification process. However, the falling leaf mode is an inherently nonlinear phenomenon and hence even the advanced linear analysis tools may not be sufficient to accurately assess the closed-loop performance. A follow-on paper[3] uses a nonlinear region of attraction analysis to compare the robustness properties of the baseline and revised control laws.

V. Nonlinear Simulation Comparison of Control Laws

Section IV compared the linear robustness properties between the baseline and the revised flight control law. However, the linear robustness analyses do not address the issue of how the flight control law will perform under the nonlinearities of the plant. Nonlinear simulation comparisons between these two flight control laws have been performed. Numerous simulations have been performed to compare the two flight control laws. Figures 22 and 23 show one such nonlinear simulation comparison between the two flight control laws. The simulation is performed by perturbing the system from the trimmed flight condition presented in

American Institute of Aeronautics and Astronautics

Table 4 for plant 4. In this specific simulation, the aileron channel has been perturbed with a doublet signal of approximately $\pm 5.50^o$ for 2 second duration. Figure 22 shows the state responses of the baseline and the revised flight control law. Notice that the revised flight control law exhibits a more damped response compare to the baseline design. Specifically, the revised control law damps out the sideslip (β) oscillation faster than the baseline design. The sideslip damping is key in suppressing the falling leaf motion.[2] Moreover, the other lateral directional states, p, r, ϕ , are also damped out faster and experience smaller deviations compared to the baseline control law. For this particular simulation, the baseline control law also exhibits larger peaks in magnitude response in the longitudinal states, α, q. Figure 23 shows the actuator dynamics response during the simulation. Notice that the baseline demands more actuation authority compared to the revised flight control law.
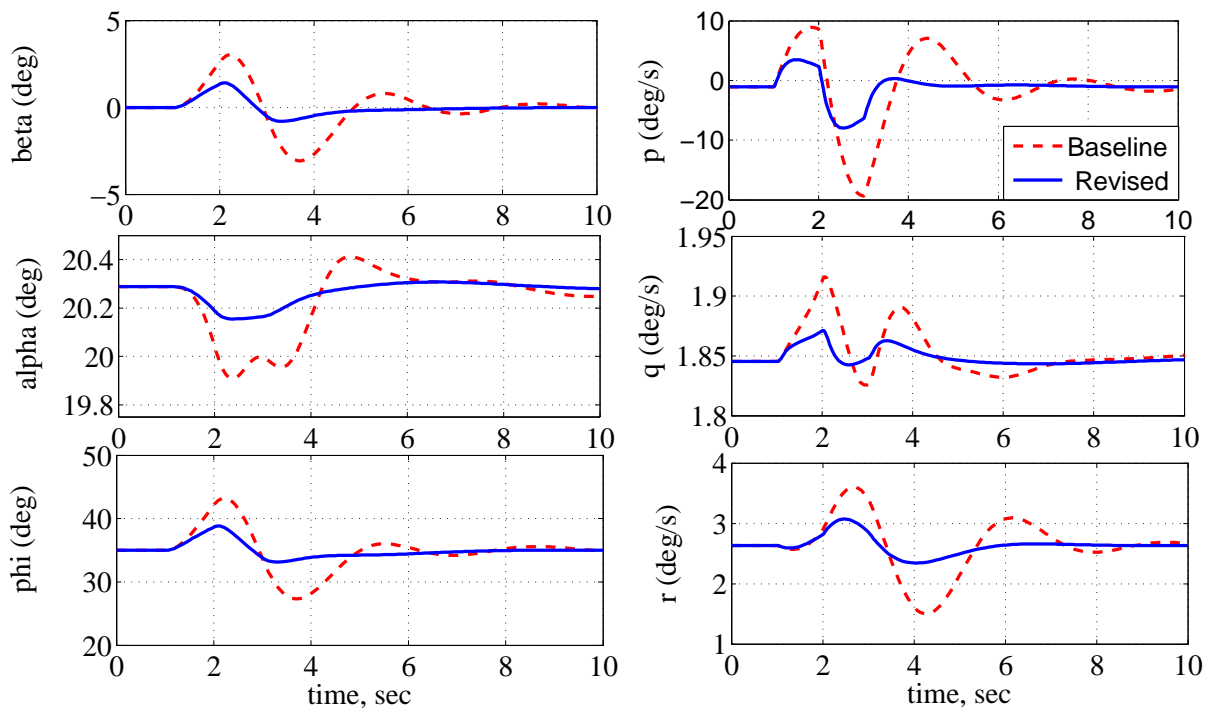

Fig. 22. Nonlinear Simulation Comparison between Baseline and Revised Flight Control Law with Perturbation in Aileron Channel

The nonlinear simulation results show that the revised flight control law is robust compared to the baseline control law design. Specifically, the characteristic of the revised controller being able to damp out the sideslip motion is key to suppressing the falling leaf motion. On the other hand, the linear analyses have not exhibited any sign of the revised controller being capable of suppressing the falling leaf motion over the baseline control law. This motivates the necessity to perform nonlinear analysis in validating the stability properties for both the control law design.
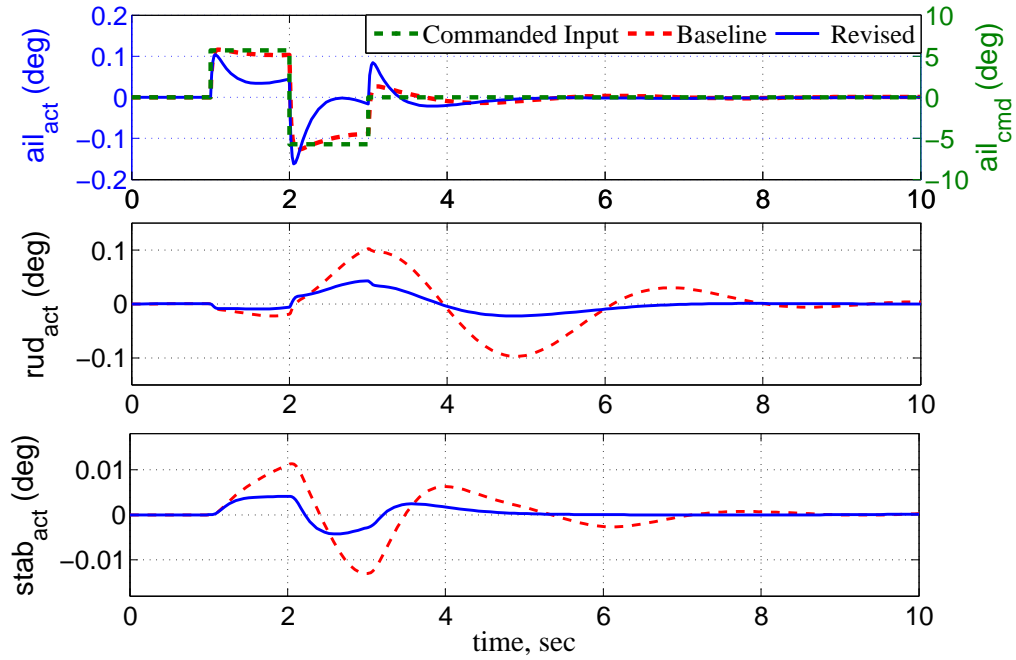
American Institute of Aeronautics and Astronautics

Fig. 23. Actuator Dynamics Comparison of Baseline and Revised Flight Control Law with Perturbation in Aileron Channel

VI. Conclusion

The F/A-18 Hornet aircraft were originally susceptible to the falling leaf mode and this necessitated the design and implementation of a revised flight control law. This paper used linear analysis tools to compare the baseline and revised F/A-18 flight control laws. Standard classical analyses, e.g. gain and phase margins, did indicated that the two control laws have similar robustness properties. In contrast, advanced linear analyses, e.g. μ analysis, indicated that the revised flight control law had significantly better robustness properties. This motivates the inclusion of advanced linear analysis tools in the validation and verification process. A follow-on paper[3] analyzes both flight control laws using nonlinear region of attraction estimation.

A. F/A-18 Full Aerodynamic Model

The aerodynamic coefficients presented here have been extracted from various papers.[5–10] The aerodynamic model of the aircraft is presented here as closed-form expression.

American Institute of Aeronautics and Astronautics

Pitching Moment, $C_m = \left(C_{m_{\alpha_2}}\alpha^2 + C_{m_{\alpha_1}}\alpha + C_{m_{\alpha_0}}\right) + \left(C_{m_{\delta_{stab_2}}}\alpha^2 + C_{m_{\delta_{stab_1}}}\alpha + C_{m_{\delta_{stab_0}}}\right)\delta_{stab}$

$$+ \frac{\bar{c}}{2V}\left(C_{m_{q_3}}\alpha^3 + C_{m_{q_2}}\alpha^2 + C_{m_{q_1}}\alpha + C_{m_{q_0}}\right)q$$

Rolling Moment, $C_l = \left(C_{l_{\beta_4}}\alpha^4 + C_{l_{\beta_3}}\alpha^3 + C_{l_{\beta_2}}\alpha^2 + C_{l_{\beta_1}}\alpha + C_{l_{\beta_0}}\right)\beta$

$$+ \left(C_{l_{\delta_{ail_3}}}\alpha^3 + C_{l_{\delta_{ail_2}}}\alpha^2 + C_{l_{\delta_{ail_1}}}\alpha + C_{l_{\delta_{ail_0}}}\right)\delta_{ail}$$

$$+ \left(C_{l_{\delta_{rud_3}}}\alpha^3 + C_{l_{\delta_{rud_2}}}\alpha^2 + C_{l_{\delta_{rud_1}}}\alpha + C_{l_{\delta_{rud_0}}}\right)\delta_{rud}$$

$$+ \frac{b}{2V}\left(C_{l_{p_1}}\alpha + C_{l_{p_0}}\right)p + \frac{b}{2V}\left(C_{l_{r_2}}\alpha^2 + C_{l_{r_1}}\alpha + C_{l_{r_0}}\right)r$$

Yawing Moment, $C_n = \left(C_{n_{\beta_2}}\alpha^2 + C_{n_{\beta_1}}\alpha + C_{n_{\beta_0}}\right)\beta$

$$+ \left(C_{n_{\delta_{rud_4}}}\alpha^4 + C_{n_{\delta_{rud_3}}}\alpha^3 + C_{n_{\delta_{rud_2}}}\alpha^2 + C_{n_{\delta_{rud_1}}}\alpha + C_{n_{\delta_{rud_0}}}\right)\delta_{rud}$$

$$+ \left(C_{n_{\delta_{ail_3}}}\alpha^3 + C_{n_{\delta_{ail_2}}}\alpha^2 + C_{n_{\delta_{ail_1}}}\alpha + C_{n_{\delta_{ail_0}}}\right)\delta_{ail}$$

$$+ \frac{b}{2V}\left(C_{n_{p_1}}\alpha + C_{n_{p_0}}\right)p + \frac{b}{2V}\left(C_{n_{r_1}}\alpha + C_{n_{r_0}}\right)r$$

Sideforce Coefficient, $C_Y = \left(C_{Y_{\beta_2}}\alpha^2 + C_{Y_{\beta_2}}\alpha + C_{Y_{\beta_0}}\right)\beta$

$$+ \left(C_{Y_{\delta_{ail_3}}}\alpha^3 + C_{Y_{\delta_{ail_2}}}\alpha^2 + C_{Y_{\delta_{ail_1}}}\alpha + C_{Y_{\delta_{ail_0}}}\right)\delta_{ail}$$

$$+ \left(C_{Y_{\delta_{rud_3}}}\alpha^3 + C_{Y_{\delta_{rud_2}}}\alpha^2 + C_{Y_{\delta_{rud_1}}}\alpha + C_{Y_{\delta_{rud_0}}}\right)\delta_{rud}$$

Lift Coefficient, $C_L = \left(C_{L_{\alpha_3}}\alpha^3 + C_{L_{\alpha_2}}\alpha^2 + C_{L_{\alpha_1}}\alpha + C_{L_{\alpha_0}}\right)\cos\left(\frac{2\beta}{3}\right)$

$$+ \left(C_{L_{\delta_{stab_3}}}\alpha^3 + C_{L_{\delta_{stab_2}}}\alpha^2 + C_{L_{\delta_{stab_1}}}\alpha + C_{L_{\delta_{stab_0}}}\right)\delta_{stab}$$

Drag Coefficient, $C_D = \left(C_{D_{\alpha_4}}\alpha^4 + C_{D_{\alpha_3}}\alpha^3 + C_{D_{\alpha_2}}\alpha^2 + C_{D_{\alpha_1}}\alpha + C_{D_{\alpha_0}}\right)\cos\beta + C_{D_0}$

$$+ \left(C_{D_{\delta_{stab_3}}}\alpha^3 + C_{D_{\delta_{stab_2}}}\alpha^2 + C_{D_{\delta_{stab_1}}}\alpha + C_{D_{\delta_{stab_0}}}\right)\delta_{stab}$$

B.   Controller Realization

The state space realization of both the baseline and the revised control laws are presented here. The controller $K = \left[\begin{array}{c|c} A_c & B_c \\ \hline C_c & D_C \end{array}\right]$ where $\dot{x}_c = A_c x_c + B_c y$ and $u_3 = C_c x_c + D_c y$ describes the controllers' state space realization with u_3 and y as described in Eq. 10 in Section IV.A.

Table 8. Aerodynamic Moment Coefficients

Pitching Moment		Rolling Moment		Yawing Moment	
$C_{m_{\alpha_2}}$ =	-1.2897	$C_{l_{\beta_4}}$ =	-1.6196	$C_{n_{\beta_2}}$ =	-0.3816
$C_{m_{\alpha_1}}$ =	0.5110	$C_{l_{\beta_3}}$ =	2.3843	$C_{n_{\beta_1}}$ =	0.0329
$C_{m_{\alpha_0}}$ =	-0.0866	$C_{l_{\beta_2}}$ =	-0.3620	$C_{n_{\beta_0}}$ =	0.0885
$C_{m_{\delta_{stab_2}}}$ =	0.9338	$C_{l_{\beta_1}}$ =	-0.4153	$C_{n_{\delta_{ail_3}}}$ =	0.2694
$C_{m_{\delta_{stab_1}}}$ =	-0.3245	$C_{l_{\beta_0}}$ =	-0.0556	$C_{n_{\delta_{ail_2}}}$ =	-0.3413
$C_{m_{\delta_{stab_0}}}$ =	-0.9051	$C_{l_{\delta_{ail_3}}}$ =	0.1989	$C_{n_{\delta_{ail_1}}}$ =	0.0584
$C_{m_{q_3}}$ =	64.7190	$C_{l_{\delta_{ail_2}}}$ =	-0.2646	$C_{n_{\delta_{ail_0}}}$ =	0.0104
$C_{m_{q_2}}$ =	-68.5641	$C_{l_{\delta_{ail_1}}}$ =	-0.0516	$C_{n_{\delta_{rud_4}}}$ =	0.3899
$C_{m_{q_1}}$ =	10.9921	$C_{l_{\delta_{ail_0}}}$ =	0.1424	$C_{n_{\delta_{rud_3}}}$ =	-0.8980
$C_{m_{q_0}}$ =	-4.1186	$C_{l_{\delta_{rud_3}}}$ =	-0.0274	$C_{n_{\delta_{rud_2}}}$ =	0.5564
		$C_{l_{\delta_{rud_2}}}$ =	0.0083	$C_{n_{\delta_{rud_1}}}$ =	-0.0176
		$C_{l_{\delta_{rud_1}}}$ =	0.0014	$C_{n_{\delta_{rud_0}}}$ =	-0.0780
		$C_{l_{\delta_{rud_0}}}$ =	0.0129	$C_{n_{p_1}}$ =	-0.0881
		$C_{l_{p_1}}$ =	0.2377	$C_{n_{p_0}}$ =	0.0792
		$C_{l_{p_0}}$ =	-0.3540	$C_{n_{r_1}}$ =	-0.1307
		$C_{l_{r_2}}$ =	-1.0871	$C_{n_{r_0}}$ =	-0.4326
		$C_{l_{r_1}}$ =	0.7804		
		$C_{l_{r_0}}$ =	0.1983		

Baseline Controller Realization

A state-space realization of the baseline controller is presented here. The baseline flight control law does not require β and $\dot{\beta}$ feedback.

$$
\left[\begin{array}{c|c} A_c & B_c \\ \hline C_c & D_c \end{array}\right] = \left[\begin{array}{c|ccccccc} -1 & 0 & 0 & 4.9 & 0 & 0 & 0 & 0 \\ \hline 0 & 0 & 0.8 & 0 & 0 & 0 & 0 & 0 \\ -1 & -0.5 & 0 & -1.1 & 0 & 0 & 0 & 0 \\ 0 & 0 & 0 & 0 & -0.8 & 0 & -8 & 0 \end{array}\right]
$$

Revised Controller Realization

A state-space realization of the revised controller is presented here.

Table 9. Aerodynamic Force Coefficients

Sideforce Coefficient		Drag Force Coefficient		Lift Force Coefficient	
$C_{Y_{\beta_2}}$ =	-0.1926	$C_{D_{\alpha_4}}$ =	1.4610	$C_{L_{\alpha_3}}$ =	1.1645
$C_{Y_{\beta_1}}$ =	0.2654	$C_{D_{\alpha_3}}$ =	-5.7341	$C_{L_{\alpha_2}}$ =	-5.4246
$C_{Y_{\beta_0}}$ =	-0.7344	$C_{D_{\alpha_2}}$ =	6.3971	$C_{L_{\alpha_1}}$ =	5.6770
$C_{Y_{\delta_{ail_3}}}$ =	-0.8500	$C_{D_{\alpha_1}}$ =	-0.1995	$C_{L_{\alpha_0}}$ =	-0.0204
$C_{Y_{\delta_{ail_2}}}$ =	1.5317	$C_{D_{\alpha_0}}$ =	-1.4994	$C_{L_{\delta_{stab_3}}}$ =	2.1852
$C_{Y_{\delta_{ail_1}}}$ =	-0.2403	C_{D_0} =	1.5036	$C_{L_{\delta_{stab_2}}}$ =	-2.6975
$C_{Y_{\delta_{ail_0}}}$ =	-0.1656	$C_{D_{\delta_{stab_3}}}$ =	-3.8578	$C_{L_{\delta_{stab_1}}}$ =	0.4055
$C_{Y_{\delta_{rud_3}}}$ =	0.9351	$C_{D_{\delta_{stab_2}}}$ =	4.2360	$C_{L_{\delta_{stab_0}}}$ =	0.5725
$C_{Y_{\delta_{rud_2}}}$ =	-1.6921	$C_{D_{\delta_{stab_1}}}$ =	-0.2739		
$C_{Y_{\delta_{rud_1}}}$ =	0.4082	$C_{D_{\delta_{stab_0}}}$ =	0.0366		
$C_{Y_{\delta_{rud_0}}}$ =	0.2054				

$$
\left[\begin{array}{c|c} A_c & B_c \\ \hline C_c & D_c \end{array} \right] =
\left[\begin{array}{c|ccccccc}
-1 & 0 & 0 & 4.9 & 0 & 0 & 0 & 0 \\
\hline
0 & 0 & 0.8 & 0 & 0 & 2 & 0 & 0.5 \\
-1 & -0.5 & 0 & -1.1 & 0 & 0 & 0 & 0 \\
0 & 0 & 0 & 0 & -0.8 & 0 & -8 & 0
\end{array} \right]
$$

C. Linear Plant

The linear plant described in Eq. 8 is provided below. This linear plant is around the trim points mentioned in Table 4 for plant 4 and plant 8. Refer to Eq. (3) for the ordering of the states and inputs.

Coordinated 35° Bank Turn: Plant 4

$$
A = \begin{bmatrix}
-6.932 \times 10^{-2} & 17.41 & -36.75 & 0 & 0 & 0 & -6.066 & -31.54 & 0 \\
-1.435 \times 10^{-4} & 2.719 \times 10^{-2} & -1.411 \times 10^{-3} & 3.467 \times 10^{-1} & 0 & -9.380 \times 10^{-1} & 7.139 \times 10^{-2} & -1.691 \times 10^{-2} & 0 \\
-4.537 \times 10^{-4} & 1.870 \times 10^{-3} & -2.025 \times 10^{-1} & 0 & 1.000 & 0 & -4.688 \times 10^{-2} & 7.563 \times 10^{-3} & 0 \\
-1.304 \times 10^{-4} & -7.179 & -4.916 \times 10^{-1} & -6.172 \times 10^{-1} & -3.689 \times 10^{-2} & 7.631 \times 10^{-1} & 0 & 0 & 0 \\
2.297 \times 10^{-5} & 0 & -8.667 \times 10^{-1} & 4.393 \times 10^{-2} & -1.947 \times 10^{-1} & -2.026 \times 10^{-2} & 0 & 0 & 0 \\
1.964 \times 10^{-5} & 4.263 \times 10^{-1} & -1.329 \times 10^{-2} & 1.233 \times 10^{-3} & 1.579 \times 10^{-2} & -1.600 \times 10^{-1} & 0 & 0 & 0 \\
0 & 0 & 0 & 1.000 & 1.941 \times 10^{-1} & 2.771 \times 10^{-1} & 0 & 6.258 \times 10^{-2} & 0 \\
0 & 0 & 0 & 0 & 8.192 \times 10^{-1} & -5.736 \times 10^{-1} & -5.615 \times 10^{-2} & 0 & 0 \\
0 & 0 & 0 & 0 & 6.055 \times 10^{-1} & 8.648 \times 10^{-1} & 0 & 2.006 \times 10^{-2} & 0
\end{bmatrix}
$$

$$B = \begin{bmatrix} 0 & 0 & -7.560 & 9.067 \times 10^{-4} \\ -6.952 \times 10^{-3} & 1.293 \times 10^{-2} & 0 & 0 \\ 0 & 0 & -3.425 \times 10^{-2} & -9.577 \times 10^{-7} \\ 4.249 & 5.989 \times 10^{-1} & 0 & 0 \\ 0 & 0 & -1.796 & 0 \\ -7.287 \times 10^{-2} & -2.877 \times 10^{-1} & 0 & 0 \\ 0 & 0 & 0 & 0 \\ 0 & 0 & 0 & 0 \\ 0 & 0 & 0 & 0 \end{bmatrix}$$

$$C = \begin{bmatrix} 0 & -5.758 \times 10^{-1} & 0 & 0 & 0 & 0 & 0 & 0 & 0 \\ 0 & 0 & 0 & 1 & 0 & 0 & 0 & 0 & 0 \\ 0 & 0 & 0 & 0 & 0 & 1 & 0 & 0 & 0 \\ 0 & 0 & 1 & 0 & 0 & 0 & 0 & 0 & 0 \\ 0 & 1 & 0 & 0 & 0 & 0 & 0 & 0 & 0 \\ 0 & 0 & 0 & 0 & 1 & 0 & 0 & 0 & 0 \\ 0 & 2.719 \times 10^{-2} & -1.411 \times 10^{-3} & 3.467 \times 10^{-1} & 0 & -9.380 \times 10^{-1} & 7.139 \times 10^{-2} & 0 & 0 \end{bmatrix}$$

$$D = \begin{bmatrix} -1.298 \times 10^{-1} & -1.610 \times 10^{-1} & 0 & 0 \\ 0 & 0 & 0 & 0 \\ 0 & 0 & 0 & 0 \\ 0 & 0 & 0 & 0 \\ 0 & 0 & 0 & 0 \\ 0 & 0 & 0 & 0 \\ -6.952 \times 10^{-3} & 1.293 \times 10^{-2} & 0 & 0 \end{bmatrix}$$

Uncoordinated 35° Bank Turn: Plant 8

$$A = \begin{bmatrix} -7.921 \times 10^{-2} & 7.516 & -35.84 & 0 & 0 & 0 & -1.914 & -32.12 & 0 \\ -1.635 \times 10^{-4} & 2.847 \times 10^{-2} & -1.650 \times 10^{-2} & 3.649 \times 10^{-1} & 0 & -9.310 \times 10^{-1} & 7.219 \times 10^{-2} & -3.414 \times 10^{-3} & 0 \\ -4.659 \times 10^{-4} & 5.902 \times 10^{-3} & -1.998 \times 10^{-1} & -1.642 \times 10^{-1} & 1.000 & -6.434 \times 10^{-2} & -4.643 \times 10^{-2} & 5.671 \times 10^{-3} & 0 \\ -1.441 \times 10^{-4} & -7.211 & -2.116 & -6.067 \times 10^{-1} & -3.938 \times 10^{-2} & 7.608 \times 10^{-1} & 0 & 0 & 0 \\ 2.667 \times 10^{-5} & 0 & -9.807 \times 10^{-1} & 4.689 \times 10^{-2} & -2.031 \times 10^{-1} & -2.487 \times 10^{-2} & 0 & 0 & 0 \\ 2.062 \times 10^{-5} & 3.995 \times 10^{-1} & -2.621 \times 10^{-1} & 1.188 \times 10^{-3} & 1.938 \times 10^{-2} & -1.607 \times 10^{-1} & 0 & 0 & 0 \\ 0 & 0 & 0 & 1.000 & 2.254 \times 10^{-1} & 3.219 \times 10^{-1} & 0 & 6.939 \times 10^{-2} & 0 \\ 0 & 0 & 0 & 0 & 8.192 \times 10^{-1} & -5.736 \times 10^{-1} & -6.011 \times 10^{-2} & 0 & 0 \\ 0 & 0 & 0 & 0 & 6.163 \times 10^{-1} & 8.801 \times 10^{-1} & 0 & 2.537 \times 10^{-2} & 0 \end{bmatrix}$$

$$B = \begin{bmatrix} -3.768 \times 10^{-1} & 7.476 \times 10^{-1} & -8.062 & 8.863 \times 10^{-4} \\ -6.106 \times 10^{-3} & 1.211 \times 10^{-2} & 4.061 \times 10^{-3} & 0 \\ 0 & 0 & -3.338 \times 10^{-2} & -1.023 \times 10^{-6} \\ 4.114 & 5.945 \times 10^{-1} & 0 & 0 \\ 0 & 0 & -1.782 & 0 \\ -7.977 \times 10^{-2} & -2.758 \times 10^{-1} & 0 & 0 \\ 0 & 0 & 0 & 0 \\ 0 & 0 & 0 & 0 \\ 0 & 0 & 0 & 0 \end{bmatrix}$$

$$C = \begin{bmatrix} 0 & -5.758 \times 10^{-1} & 0 & 0 & 0 & 0 & 0 & 0 & 0 \\ 0 & 0 & 0 & 1 & 0 & 0 & 0 & 0 & 0 \\ 0 & 0 & 0 & 0 & 0 & 1 & 0 & 0 & 0 \\ 0 & 0 & 1 & 0 & 0 & 0 & 0 & 0 & 0 \\ 0 & 1 & 0 & 0 & 0 & 0 & 0 & 0 & 0 \\ 0 & 0 & 0 & 0 & 1 & 0 & 0 & 0 & 0 \\ 0 & 2.847 \times 10^{-2} & 1.650 \times 10^{-2} & 3.649 \times 10^{-1} & 0 & -9.310 \times 10^{-1} & 7.219 \times 10^{-2} & 0 & 0 \end{bmatrix}$$

$$D = \begin{bmatrix} -1.298 \times 10^{-1} & -1.610 \times 10^{-1} & 0 & 0 \\ 0 & 0 & 0 & 0 \\ 0 & 0 & 0 & 0 \\ 0 & 0 & 0 & 0 \\ 0 & 0 & 0 & 0 \\ 0 & 0 & 0 & 0 \\ -6.106 \times 10^{-3} & 1.211 \times 10^{-2} & 4.061 \times 10^{-3} & 0 \end{bmatrix}$$

Acknowledgments

References

References

[1]Jaramillo, P. T. and Ralston, J. N., "Simulation of the F/A-18D falling leaf," *AIAA Atmospheric Flight Mechanics Conference*, 1996, pp. 756–766.

[2]Heller, M., David, R., and Holmberg, J., "Falling leaf motion suppression in the F/A-18 Hornet with revised flight control software," *AIAA Aerospace Sciences Meeting*, No. AIAA-2004-542, 2004.

[3]Chakraborty, A., Seiler, P., and Balas, G., "Susceptibility of F/A-18 Flight Control Laws to the Falling Leaf Mode Part II: Nonlinear Analysis," *AIAA Guidance, Navigation, and Control*, 2010.

[4]Buttrill, S. B., Arbuckle, P. D., and Hoffler, K. D., "Simulation model of a twin-tail, high performance airplane," Tech. Rep. NASA TM-107601, NASA, 1992.

[5]Napolitano, M. R., Paris, A. C., and Seanor, B. A., "Estimation of the longitudinal aerodynamic parameters from flight data for the NASA F/A-18 HARV," *AIAA Atmospheric Flight Mechanics Conference*, No. AIAA-96-3419-CP, pp. 469–478.

[6]Napolitano, M. R., Paris, A. C., and Seanor, B. A., "Estimation of the lateral-directional aerodynamic parameters from flight data for the NASA F/A-18 HARV," *AIAA Atmospheric Flight Mechanics Conference*, No. AIAA-96-3420-CP, 1996, pp. 479–489.

[7]Lluch, C. D., *Analysis of the Out-of-Control Falling Leaf Motion using a Rotational Axis Coordinate System*, Master's thesis, Virginia Polytechnic Institue and State Unniversity, 1998.

[8]Iliff, K. W. and Wang, K.-S. C., "Extraction of lateral-directional stability and control derivatives for the basic F-18 aircraft at high angles of attack," *NASA TM-4786*, 1997.

[9]Napolitano, M. R. and Spagnuolo, J. M., "Determination of the stability and control derivatives of the NASA F/A-18 HARV using flight data," Tech. rep., NASA, 1993.

[10]Carter, B. R., *Time optimization of high performance combat maneuvers*, Master's thesis, Naval Postgraduate School, 2005.

[11]Illif, K. W. and Wang, K.-S. C., "Retrospective and recent examples of aircraft parameter identification at NASA Dryden Flight Research Center," *Journal of Aircraft*, Vol. 41, No. 4, 2004.

[12]Foster, J. V., 2009.

[13]Stevens, B. and Lewis, F., *Aircraft Control and Simulaion*, John Wiley & Sons, 1992.

[14]Stengel, R., *Flight Dynamics*, Princeton University Press, 2004.

[15]Cook, M., *Flight Dynamics Principles*, Wiley, 1997.

[16]Heller, M., Niewoehner, R., and Lawson, P. K., "High angle of attack control law development and testing for the F/A-18E/F Super Hornet," *AIAA Guidance, Navigation, and Control Conference*, No. AIAA-1999-4051, 1999, pp. 541–551.

[17]Balas, G., Chiang, R., Packard, A., and Safonov, M., *Robust Control Toolbox*, MathWorks, 2008.

[18]Heller, M., Niewoehner, R., and Lawson, P. K., "On the Validation of Safety Critical Aircraft Systems, Part I: An Overview of Analytical & Simulation Methods," *AIAA Guidance, Navigation, and Control Conference*, No. AIAA 2003-5559, 2003.